Summer 2018

Non-Destructive Evaluation for Composite Material

Desalegn Temesgen Delelegn
Old Dominion University

NON-DESTRUCTIVE EVALUATION FOR COMPOSITE MATERIAL

by

Desalegn Temesgen Delelegn
B.S. July 2010, Mekelle University, Ethiopia

A Thesis Submitted to the Faculty of
Old Dominion University in Partial Fulfillment of the
Requirements for the Degree of

MASTER OF SCIENCE

ELECTRICAL AND COMPUTER ENGINEERING

OLD DOMINION UNIVERSITY
August 2018

Approved by:

Jiang Li (Director)

Dimitrie C. Popescu (Member)

Masha Sosonkina (Member)

William P. Winfree (Member)

ABSTRACT

NON-DESTRUCTIVE EVALUATION FOR COMPOSITE MATERIAL

Desalegn Temesgen Delelegn
Old Dominion University, 2018
Director: Dr. Jiang Li

The Nondestructive Evaluation Sciences Branch (NESB) at the National Aeronautics and Space Administration (NASA) Langley Research Center (LaRC) has conducted impact damage experiments over the past few years with the goal of understanding structural defects in composite materials. The Data Science Team within the NASA LaRC Office of the Chief Information Officer (OCIO) has been working with the Non-Destructive Evaluation (NDE) subject matter experts (SMEs), Dr. Cheryl Rose, from the Structural Mechanics & Concepts Branch and Dr. William Winfree, from the Research Directorate, to develop computer vision solutions using digital image processing and machine learning techniques that can help identify the structural defects in composite materials.

The research focused on developing an autonomous Non-Destructive Evaluation system which detects, identifies, and characterizes crack and delamination in composite materials from computed tomography (CT scans) images. The identification and visualization of cracking and delamination will allow researchers to use volumetric models to better understand the propagation of damage in materials, leading to design optimizations that will prevent catastrophic failure.

ACKNOWLEDGEMENTS

TABLE OF CONTENTS

LIST OF TABLES

LIST OF FIGURES

CHAPTER 1

INTRODUCTION

The Advanced Composite Program at NASA LaRC(Langley Research Center) has conducted impact damage experiments over the past few years with the goal of understanding damage growth in composite materials. The Data Science Team within the NASA LaRC Office of the Chief Information Officer (OCIO) has been working with the NDE subject matter experts (SMEs) to develop automatic techniques that can help identify and characterize structural defects in composite materials.

The research goal is to develop algorithms to automatically and rapidly detect and locate various types of anomalies, delamination, crack and fiber breakage, in X-Ray/CT data of laminated composite structures. This thesis focus has been on segmenting structural defects, especially delamination and cracks, within the composite material using machine learning and digital image processing. Achieving the project goal will save SMEs time and effort by eliminating the need to manually identify and segment the structural defects in the material and allow them to focus on the development of finite-element models for residual strength analysis.

1.1 Background on Composite Material Especially Carbon Fiber.

Carbon is one of the most abundant elements and has been used since ancient times in the form of charcoal, graphite, and diamonds[1]. The carbon technology can be traced in a chronological order starting from the first "lead" pencils in the 1600ś to the industrial production of chemical vapor deposition (CVD) diamonds in 1992. But, according to J. Gorss[2], the modern era of carbon fibers started back in 1956 in Parma, OH by Union Carbide; now part of GrafTech International; at the Parma Technical Center.

Figure 1 shows a comparison between human hair and carbon fiber in diameter, the image was obtained from reference [3]. After decades of researches and manufacturing improvements, the modern day commercial carbon fibers come from one of the three kinds of precursor materials which are, [2]:
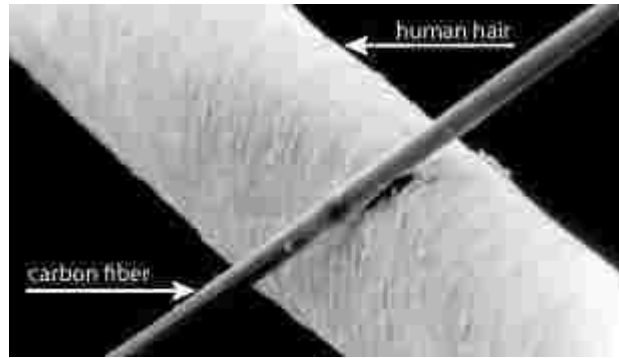
Fig. 1: Carbon fiber thickness in comparison with human hair.

- **Rayon** which saw its first commercial production in 1959;

- **Polyacrylonitrile (PAN)** based which fueled the explosive growth of the carbon fiber industry since 1970 and also still widely used in various industries; or

- **Pitch-based** which has fibers that are unique in their ability to achieve ultra-high Young's modulus and thermal conductivity which are critical in military and space applications.

Currently, carbon fiber reinforced materials are used in automobile, airplanes, space aircraft structures, military, lithium batteries, sporting goods, and structural reinforcement in construction materials[2]. As the carbon fiber commercial production and inspection techniques gets simpler, cheaper, more efficient, and faster, it is safe to say that carbon fiber materials will be the future building blocks due to their superior strength per unit mass and heat resistance.

Carbon fiber materials are strong but as any other materials, they have their own limits. And, any damage they face can generally be divided into three; depending on when in their lifetime cycle the damage occurred. These lifetime cycles are during the manufacturing of the fibers, or during the construction of the composite, or during the in-service life of the composite[4].

1.2 Background on NDE Evaluation
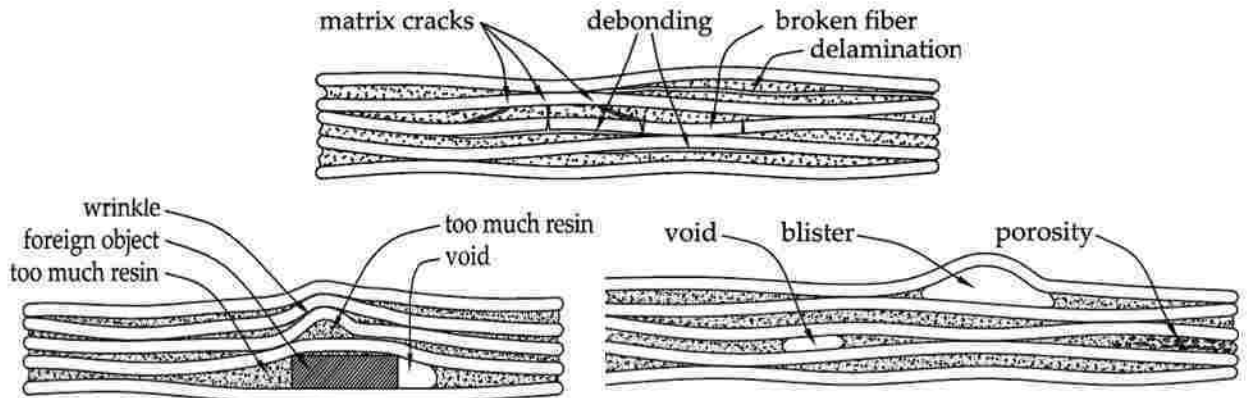
Fig. 2: Shows various damages in a composite material[4].

An interest of researchers has been to get the most available insights out of their experiments to understand materials' properties and their limits. Scientists and researchers have been using different methods in determining the physical properties; which includes Young's modulus, corrosion resistance, hardness, tensile strength, impact strength, and *e.t.c*; of a material or evaluate the material's conditions; in case of graphite fiber reinforced polymers this includes delamination, crack, and breakage of fibers; under observation. To assess their performance, both destructive and nondestructive methods are utilized.

The non-destructive method has been used in the material science field for several decades. However, there is an increasing interest in monitoring, identifying and quantizing defects in graphite fiber reinforced polymer in real-time speed. To do this kind of analysis, researcher need better and reliable techniques and fast algorithms. There are a number of NDE techniques starting from the simplest coin tapping, vibration based, visual test and thermal infrared testing [4]. Our focus is to use CT scan images to identify defects in graphite fiber reinforced polymer material which we discussed and implemented in the coming sections.

1.3 Background on X-ray Computed Tomography (CT) Scan

X-ray imaging is best known in the medical field for diagnosis. But, let's first discuss how this representation and analysis are possible.

Artificial X-ray beams, whether medical or industrial, are generated by high speed

electrons traveling from a heated cathode to a positively charged anode; which are encapsulated in a vacuum tube. When the high speed electrons strike the anode, they release energy as a form of X-ray radiation. The x-ray energy is controlled by varying the anode voltage and the current to the filament in the cathode which controls the x-ray intensity[5].

This section briefly covers how the CT X-ray scan in material science has become one of the most accepted tools in non-destructive evaluation of composite materials. And, there is no better literature to start with other than the book edited by John Banhart[6]. This reference is very detailed and gives abundant coverage on the history, mathematical concepts, visualization, processing, analysis, and a lot more on tomographic data. For our case, let's start with the definition of Computed Tomography (CT). The word tomography derived from two greek words tomos; meaning to section or slice; and graphein; meaning to write. And, the word computed indicates the method how the X-ray images are obtained.

1.3.1 Computed Tomography Principles

CT scanning devices use *radiation imaging.* A radiation imaging device works with a principle that is based on capturing the interaction between particles such as protons, electrons, neutrons, or other modalities such as sound waves and an object under consideration. The interaction of these particles' rays with the object can result in simple attenuation, shift in phase, deflect, scatter, or change in energy of the rays; which then can be monitored and recorded[6]. Additionally, the incoming ray exciting particles in the object which sends out their own radiation which then can be recorded and monitor.

1.3.2 Computed Tomography Imaging Principles

According to J. Banhart[6], the most simple and effective way of radiation imaging is X-ray radiography which works by imaging the attenuation of the X-rays as they interact with the electrons of the material. Then, the object is represented in a two-dimensional (2D) image on the detector which are acquired as the projected electron density in the object.

One of the short comings of this technique at the early stage was, that objects which are inline directly along an x-ray beam would be independently imaged in the two-dimensional (2D) image representation as the objects are superimposed.

Fig. 3: One of the first ever X-ray images by W.C. Röntgen[6].

Thanks to Godfrey N. Hounsfield medical tomography invention, by rotating the object through 360° with a constant angle increment and capturing the 2D representations, the objects can be independently imaged. A mathematical reconstruction algorithm developed first by Johann Radon(1917) and then Allan Cormack (1963)[6] is applied that approximates the X-ray attenuation coefficients of any spatial volume inside the object.
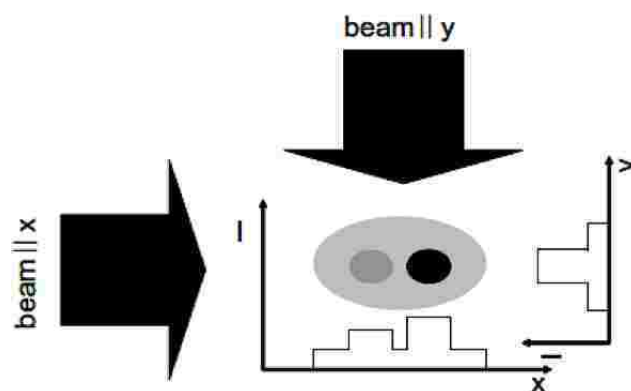
Fig. 4: Scanning an object from different directions which has three different dense structures[6].

By the late 1970s, scanning of non-living objects with computed tomography (CT)

started which paved the way for larger industrial X-ray tomography. Even though CT was effective for industrial problems due to the high fidelity in representing 3D objects' internal structures, it was too expensive and slow for routine application.

- small objects
- dose mostly not critical
- slow
- quantitative, element sensitive
- high resolutions ≈ 1μm or below
- energy < 50 keV

- Large objects
- Dose limitations
- Fast
- Low resolutions ≈ 1mm
- Energy < 200 keV

- large objects
- dose not critical
- fast
- low resolutions ≈ 1mm
- energy < 300 keV
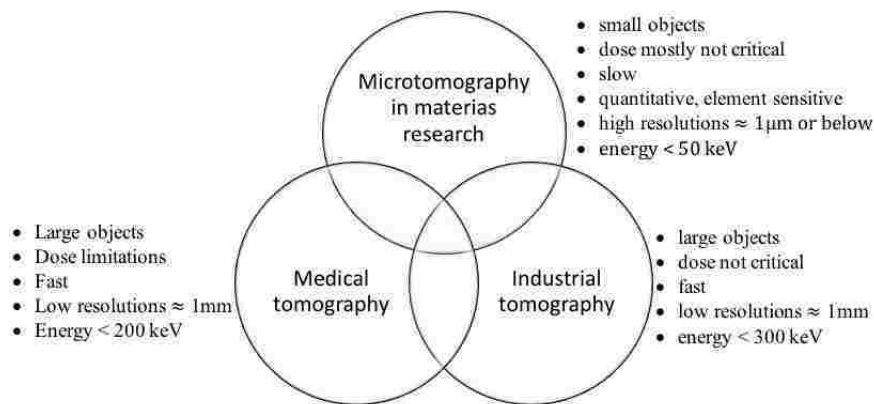
Fig. 5: Comparison between different X-ray tomographies redrawn from [6].

1.4 Digital Image Processing in Non-Destructive Evaluation

Digital image processing is one of the most studied and actively researched fields in electrical engineering. The first application of digital image was witnessed when pictures were sent between London and New York via a submarine cable in the first quarter of the 20th century. R. C. Gonzalez and R. W. Woods[5] stated that the main goal of digital image processing was to improve digital images' quality for a better human interpretation and to process image data for storage, transmission, and interpretation by autonomous machine perception.

Digital image processing application can easily be found in digital smart phones and TV sets we interact with. If you have a smart phone, you are utilizing the powerful advantage of digital image processing. It could be you taking a picture using your phone camera, or checking the price of an item using one of the handful apps, for example, Amazon shopping app, or it could be accessing a company website using their Quick Response (QR) code identity. These are some of the obvious ones, not to mention every social media platform with their image filters.

Recently, B. Bauer and *et al*[7], in their 2017 article applied image segmentation techniques; to include the time tested and famous Otsu's threshold method; to segment bi-pores from soil CT images. But, the main focus here is to exploit the

potential of digital image processing to identify cracks and delamination and quantify the extent of the damage in a carbon fiber reinforced polymer, which we cover extensively in the methodology chapter.

Digital image processing has been used extensively in the material science starting from W. Krakow[8] to R. Leach [9] for materials' structure characterization. In the year 2000, M.L. Comer and E.J. Delp[10] implemented digital image processing for simultaneous parameter estimation and segmentation of textured images.

Following their footsteps and all the other unsung heroes who implemented digital image processing techniques in analyzing CT images, we implemented digital image filtering and transformation using Haar wavelet transform for our innovative approach to come up with a better segmentation which we discuss in detail in chapter 3.

1.4.1 Haar Wavelet Transform.

Image processing and analysis based on the continuous or discrete image transforms has been implemented for a long time. But, the wavelet transform is now making it even easier to compress, transmit, and analyze many images. Wavelets are powerful in analyzing the local frequency and time behavior of signals. Fourier analysis of functions require many coefficients to represent the signal in the Fourier domain. Wavelets analysis can provide accurate representation of such signals with excellent reconstruction of the original signals with fewer coefficients since wavelets functions are compact functions. Here, the Discrete Wavelet transform (DWT), especially using Haar wavelets, is introduced. The Haar wavelets, which are the simplest wavelets forms, are used here to generate the sub-images which we discuss in detail in chapter 3.

The Haar transformation basis functions are the oldest and simplest known orthonormal wavelets and used here for the extraction of sub-image based features. Mathematically, the Haar transform is expressed as:

$$F = HfH_t \tag{1}$$

Where, f is an $N \times N$ image matrix, H is an $N \times N$ Haar transformation matrix, and F is the resulting $N \times N$ transformation. H_t is the transpose of H since H is not symmetric. If you notice, all matrices are a square matrices on purpose to ease the generation of wavelet coefficients you will see in the coming section.

For the Haar transform, H contains the Haar basis functions, $h_k(z)$, and are defined over the continuous, closed interval $z\epsilon[0,1]$ for $k = 0, 1, 2, ..., N - 1$, where $N = 2^n$. H can be generated by defining the integer k such that $k = 2^p + q - 1$, where $0 \leq p \leq n-1$, $q = 0$ or $p = 0$, and $1 \leq q \leq 2^p$ for $p \neq 0$. Then, the Haar basis functions are:

$$h_0(t) = 1/\sqrt{N}$$

$$h_k(t) = \frac{1}{\sqrt{N}} \begin{cases} 2^{p/2} & (q-1)/2^p \leq t < (q-0.5)/2^p \\ -2^{p/2} & (q-0.5)/2^p \leq t < q/2^p \\ 0 & \text{otherwise} \end{cases}$$

The i_{ith} row of an $N \times N$ Haar transformation matrix contains the element of $z = \frac{0}{N}, \frac{1}{N}, \frac{2}{N}, ..., \frac{n-1}{N}$.

1.4.2 Wavelet Transform in Two Dimensions.

In two dimensions, a two-dimensional scaling functions, $\varphi(x, y)$, and three two-dimensional wavelets, $\psi^H(x, y), \psi^V(x, y), and \psi^D(x, y)$, are required. Each is the product of two one dimensional functions. Excluding products that produce one-dimensional results, the remaining four products give separable scaling functions and separable "directionally sensitive" wavelets which are expressed as:

$$\psi^H(x, y) = \psi(x)\varphi(y) \tag{2}$$

$$\psi^V(x, y) = \varphi(x)\psi(y) \tag{3}$$

$$\psi^D(x, y) = \psi(x)\psi(y) \tag{4}$$

Where, $\psi(x)$ and $\psi(y)$ are the wavelets along x- and y- direction, respectively. $\varphi(x)$ and $\varphi(y)$ are the scaling functions in their respective directions. The above wavelets measure functional variations-intensity variations for images along the respective directions as $\psi^H(x, y)$ for horizontal, $\psi^V(x, y)$ for vertical, and $\psi^D(x, y)$ for diagonal. The F in equation 1 contains the separable "directionally sensitive" wavelets as seen in figure 6.

1.5 Background on Convolutional Neural Network(CNN)

Machine learning, as you might have heard it commonly referred to as artificial intelligence, has been around for a long time before it suddenly engulfed different
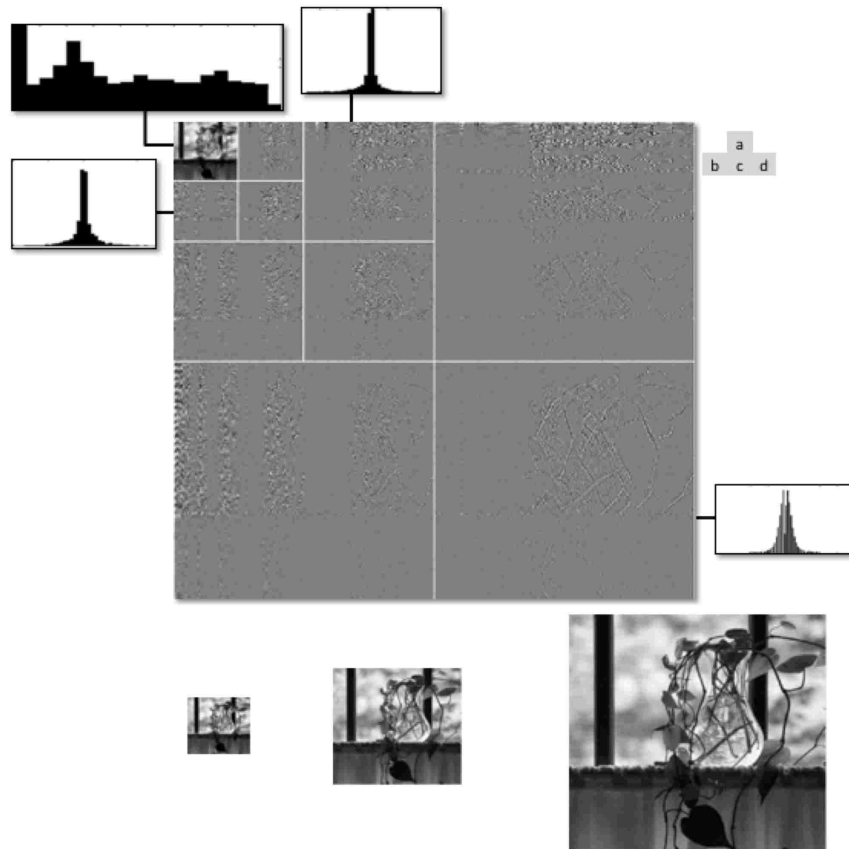
Fig. 6: (a) A discrete wavelet transform using Haar transform H_512 and its local histogram variations. (b)-(d) several different approximations (64×64, 128×128, and 256×256) that can be obtained from (a). Modified and regenerated from the book by R.C. Gonzalez and R. W. Woods[5].

disciplines like a wild fire. In todays environment, businesses make decisions by using every little detail that are available to them to get the edge they needed. This requires the decision making process to be fast and accurate without compromising the bottom line. This demand with faster and improved computational computers capability like Graphics Processing Unit (GPU) made it possible for machine learning tools to develop faster and more efficiently. As machine learning exploits the underline statistical details of data, this makes it more attractive to tackle most scientific and financial problems. You do not need to look further than your pocket to find applications of machine learning in 2018. To mention some of them, Alexa, Siri, or the 3D face emojis on the newer phones, or even better unlocking your phone

with your finger prints, which has been around for quite some time; but the pace of advanced technology made it look like an ancient technology.

Convolutional Neural Network(CNN) sometimes referred to as ConvNet is a feed-forward neural network which has been implemented intensively in pattern recognition and computer vision problems. A typical CNN is constructed from multilayer perceptrons which ideally require minimum preprocessing of input data. The minimal preprocessing requirement comes from the network perceptrons ability to learn, "design" and optimize their own filters' coefficients, which used to be optimized and implemented by engineers in a manual fashion.

Normally, a CNN model has input layer, then hidden layer(s), and lastly output layer. The input and the output layers are the same to most CNN based models with the exception of their vector dimensions. Commonly, hidden layers are made of a combination of convolutional, pooling, activation(normalizing), dropout, and fully connected layers. This is where one can mix-and-match and tune the kernel parameters to their own flavor to model the best of performing model architecture towards a specific problem.

- **Convolutional Layer**: used for applying a convolution on their input and pass the result to their respective receptive output layer.

- **Pooling Layer**: combines outputs from one layer and passes to the next layer as a single neuron, either by local or global pooling. Mostly implemented as maximum or average.

- **Activation layer**: introduces a nonlinearity transform between layers. Typical, this layer is added after each convolutional layer. The output of this layer decides which neuron to activate on the next layer. Examples, Rectified Linear Units(ReLU), Sigmoid, which are implemented in our approach.

- **Dropout layer**: This is a result of recent developments to prevent overfitting of the network which has weights too tuned to learn the training data perfectly. Thus, a set of randomly selected neurons in a specific layer are set to zero during training.

- **Fully Connected Layer**: Here, all the neurons are connected with another layer's neuron in a weighted manner, which can be considered as a multiple perceptron neural network. Each weighting is optimized during training phase.

The more fully connected layers added to a model, the more computationally expensive it gets.

The application of neural network in image processing can be traced back to 1992 when L.O. Hall and *et al*[11] developed an image segmentation algorithm for Magnetic resonance(MR) brain section images by implementing the literal and approximate fuzzy c-means unsupervised clustering algorithms and a supervised computational neural network, a dynamic multilayered perception trained with the cascade correlation learning algorithm.

In the NDE arena, researchers implemented machine learning techniques in combination with digital image processing, as almost all of image recognition problem do in recent years, to get promising results. S. Sarkar[12] paper implemented deep learning, one of the machine learning algorithms, to characterize the damage in the form of cracks in a composite material. Figure 11 shows their implementation frame work they used to characterize damage.

Ruggiero, C., Ross, A. and Porter, R.[13] surveyed image segmentations, which included supervised machine learning that provided interactive tools to learn from the operators' input over longer periods of time. They insisted that user inputs can be utilized in two main ways, as inference and learning, by breaking the segmentation workflow into three stages, named as S0, S1, and S2 as seen in figure 7.
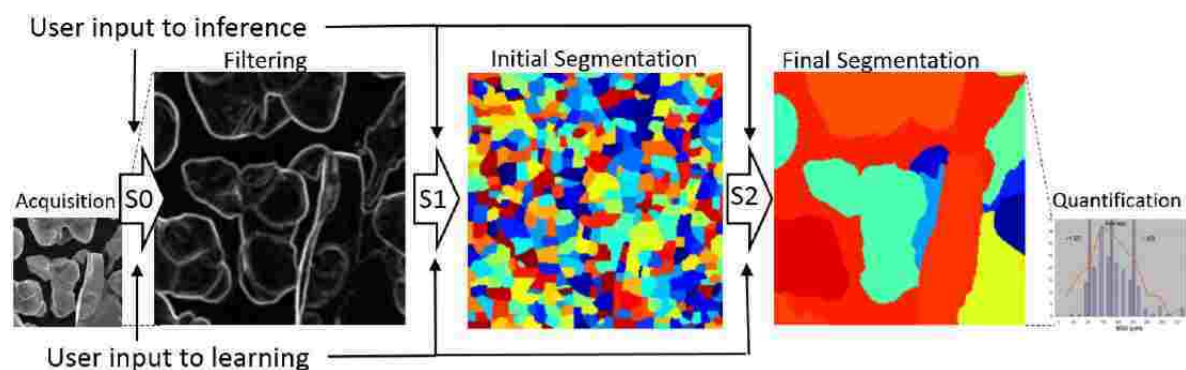
Fig. 7: User input to image analysis workflow implemented by Ruggiero, C., Ross, A. and Porter, R.[13]

When A. Krizhevsky, I. Sutskever and G.E. Hinton[14] implemented a deep CNN to classify the 1.2 million ImageNet's images into 1000 different classes, it caught the world of CNN by storm. It was one of the most significant highlights of CNN model

architecure. Their model was able to classify remarkably with very high accuracy.

1.6 Background on LaRC's NDE Research

The Advanced Composites Program at NASA LaRC has conducted impact damage experiments over the past few years with the goal of understanding structural defects in composite materials. The Data Science Team at Langley Research Center (LaRC) has been working with the NDE subject matter experts (SMEs) to develop automatic techniques that can help identify the structural defects in composite materials.

C.D. Lockard[15] in his 2015 master thesis worked under Data Science team; the then Big Data and Machine Intelligence initiative; in collaboration with Dr. William Winfree and Eric Burke introduced a regression-based algorithm for identifying anomalies in the grayscale CT images. Previously, researchers manually segmented the CT images, which are labor intensive and have a very inefficient processing time. Based on T. Chan and L. Vese[16] anomaly detection work, Dr. Winfree wrote MATLAB source codes which took four setting parameters and required the SMEs to perform trial-and-error runs to achieve an acceptable segmentation.

1.7 Problem Statement

The research has been carried out in collaboration with Dr. Cheryl Rose (Structural Mechanics & Concepts Branch) and Dr. William Winfree (Research Directorate) with the data science team, which is under OCIO, to develop autonomous non-destructive evaluation (NDE) system, which detects, identifies, and characterizes crack and delamination in composite materials from computed tomography (CT scans) images based on machine learning, especially CNN, and digital image processing. Identification and visualization of cracking and delamination will allow researchers to use structural analysis models to better understand the propagation of damage in materials, leading to design optimizations that will prevent catastrophic failure.

CHAPTER 2

BACKGROUND OF THE STUDY

2.1 Literature Review

Many research studies have been conducted surrounding carbon fiber reinforced polymers from manufacturing to inspection. The manufacturing part of the research started well before the 21st century. But, as carbon fiber materials became more relevant in the military, auto, space, and sporting goods industries, the demand to inspect and certify their service life grew with their applications. In addition, these techniques need to be reliable and fast and if possible, perform early detection to prevent the catastrophic failure of carbon fiber composite materials. Researchers have used different NDE techniques, which were covered under section 1.2, to identify and characterize defects in composite material.

V. Hugo and *et al*[17] in their 2008 paper, presented an evaluation of the effect of delamination on the performance of composite materials, particularly fiber reinforced plastics, due to drilling which are inherent to most of manufacturing and assembling processes. In their investigation, the focus was to evaluate the degree and the effect of delamination on the composite material by identifying and characterizing the delaminated area within images which were obtained from radiograph. To solve this task, they implemented digital image processing and back propagation artificial neural network techniques.

Hugo and *et al* modeled two delamination damages, peel-up and push-down delamination, which are prominent to fiber reinforced plastics composite during drilling, shown in figure 8 and their algorithm implementation scheme in figure 9.

Hugo and *et al* were able to get results shown in figure 10 with their implementation. They asserted that damage around the pilot holes, especially delamination between inner plies of the laminate, can be evaluated best by using enhanced radiography. But, they implied that the method is only possible if parts are immersed in a contrasting fluid.

In another recent development, S. Sarkar and *et al*[12] in their characterization of damage research implemented deep learning architecture with multi-layer neural
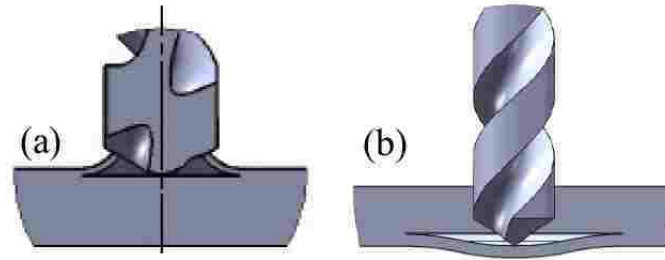
Fig. 8: Type of delamination. (a)Peel-up and (b) Push-out [17]
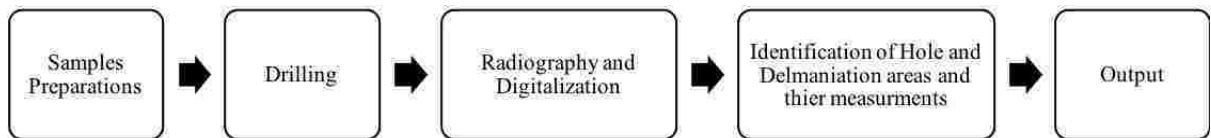
Fig. 9: Block diagram (modified) that was implemented by Hugo and *et al.* **Note:** Block diagram modified without obscuring the intended flow for presentation purpose only. Refer [17] for the original block diagram.
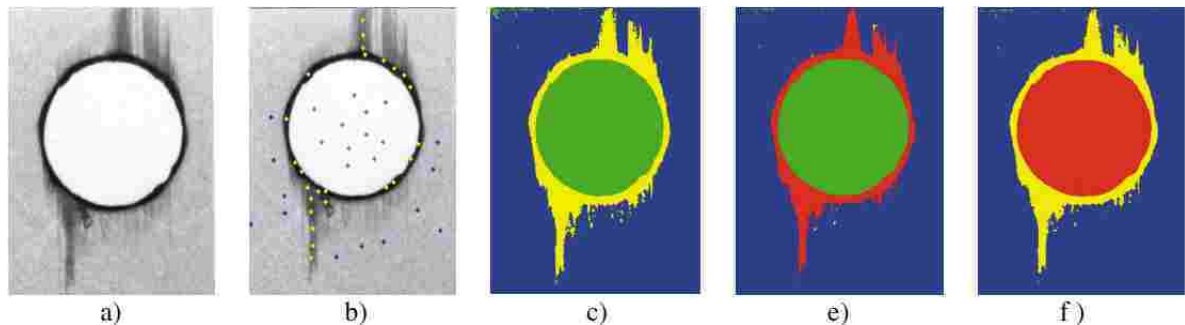
Fig. 10: Areas identification and measurements: a) original image; b) pixels selection for the training phase; c) segmentation results; final results (in red), d) delaminated region and e) hole region[17] .

network based on the unsupervised representational learning theory. The framework of their implementation can be seen in figure 11. Their research focused on addressing extensive heuristics for parameter tuning in existing vision-based crack detection.
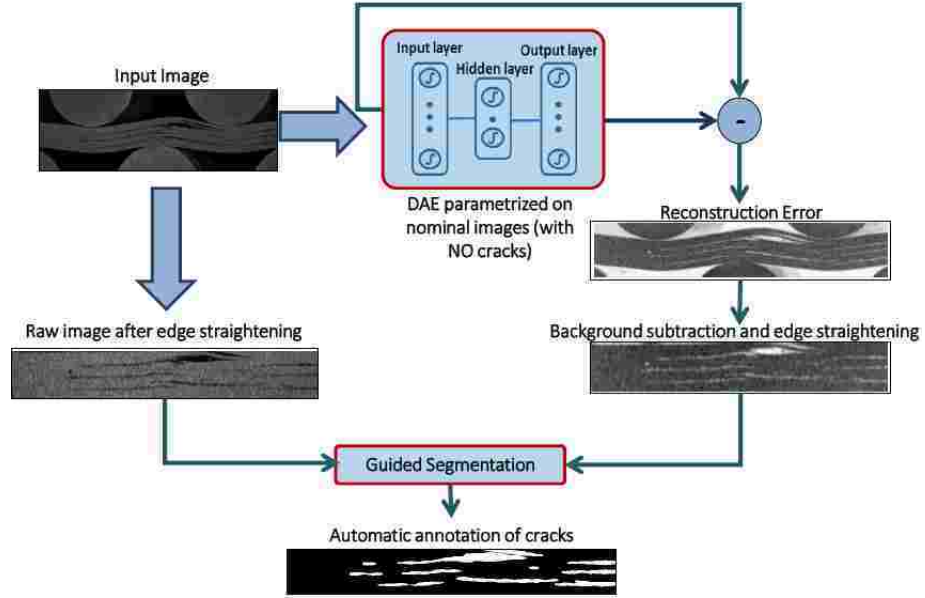
Fig. 11: Damage characterization framework[12].

S. Sarkar and *et al* recorded a video of the material under observation while bending the coupon under steady increasing stress until full fracture then used the images from the video frames as their starting point. Then, they applied the developed framework to automatically detect and annotate the cracks in real-time. At the end, they presented the final segmentation output as the crack length distribution which they considered as the damage characterization measuring metrics.

S. Sarkar and *et al* believed the number of cracks correctly detected and the normalized distance between original and estimated distribution of the crack lengths should be used as a performance metrics rather than the number of pixels detected correctly. Their experimental result is shown in table I .

Loading level	Number of correct Loading level cracks detected	Estimated distribution of crack lengths d
low	4 out of 4	0.18
medium	16 out of 17	0.1
high	19 out of 20	0.15

TABLE I: Damage characterization performance of Sarkar and *et al* model[12]

Sarkar and *et al* concluded by mentioning their future work as:

- formulate and implement an end-to-end (from image frame to damage characterization) deep learning architecture by eliminating the separate guided segmentation module.

- parametric tracking of non-linear topological deformation instead of heuristic edge straightening.

- applying 3D convolutional deep auto-encoder(DAE) for 3D damage characterization.

M. Krumm and *et al*[18] in their 2012 paper started by hinting that fiber composites are not yet used in mass production as several questions of automatic production and testing are still open. They also stated that testing methods which allow complete material characterization and non-destructive troubleshooting with adequate effort are still a field of current research; but they suggested that X-ray CT images can deliver an alternative way of measuring damages due to the fact that CT images can contain exact 3D cross-sectional imaging of an object. They collected the 3D images by a method referred as 3D-CT; which is 3D computed tomography.
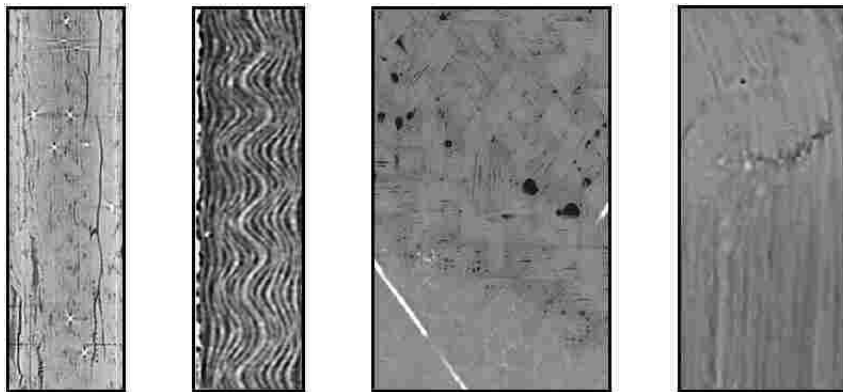
Fig. 12: Damage types. From left to right: delamination, undulation, porosity and fibre crack[18].

M. Krumm and *et al* were able to assess the damages and concluded by stating that typical errors and damage patterns of fiber component materials can be measured and visualized very well in most cases[18].

X. Liu and F. Chen[19] in their 2016 article investigated the effect of resolution on the accuracy of defects estimation during carbon fiber reinforced plastic (CFRP) damage assessment. X-ray CT images were used in their research in conjunction with

previous work; which asserted that the mechanical properties of CFRP structures are affected by both the location of delamination and its size; to capture the entire 3D information of the damage. They commented that the X-ray CT ability to give entire 3D information makes it a great candidate if the focus is to assess internal damage of a composite material.

M.F. Pernice and *et al*[20] studied the delamination migration in composite laminates. In this 2015 article, they were able to find a correlation between the numerical results and experimental observations. From this observation, they concluded that the deciding factor for delamination to progress near the interface along the ply plane or migrate through the neighboring ply depends on the shear stress sign at the delamination front, combined with the fiber direction of the bounding plies, dictates whether delamination will propagate near the interface along the ply direction, or migrate through the neighboring ply.

M.F. Pernice and *et al* were also able to observe that the migration process of delamination is inherent to delamination between plies of dissimilar orientation, it is suggested to take dissimilar orientation into account during simulation of damage propagation in tape laminates. They concluded their paper by eliciting that their results provide a validation data for modeling and capturing delamination migration.

In 2017, E.Yılmaz and *et al* published an article titled characterization of the damage mechanism of composites against low velocity ballistic impact using computed tomography (CT) techniques[21], seen in figure 13.

E.Yılmaz and *et al* also observed that the major energy absorption for the instant impact was the micro-cracking of the matrix resulting in the breakage of the fibers. They utilized CT images to visualizes the full extent of the damage progression in 3-D.

There have been more developments, [22]-[34], in implementing CT scanned images to assess damage and quantify their extent. But, to the best of our knowledge there is no automated implementation of NDE techniques utilizing X-ray CT scan, machine learning and digital image processing algorithms to identify cracks and delamination in composite materials. One thing to note is that most of the techniques rely on subject matter expert visual inspection of the images to determine the extent of damage in the composite material. In our research, we developed a technique to identify and segment out cracks and delamination in automated and fast fashion with minimum SMEs involvement by implementing machine learning and digital image

Fig. 13: Surface panel following a 9mm shot[21].

processing techniques.

The approach we implemented is novel as it accounts for both types of damages, crack and delamination, considers the 3D CT images from 2D and 3D stand points, requires no or minimum interaction from the SMEs, and has fast detection and segmentation which is inline with the efficient inspection of carbon fiber materials.

2.2 Description of The Study Sample

The experiments were carried out by K. Song, F.A. Leone and C.A. Rose[22]. They considered four flat composite test panels. The test panels were comprised of Hexcel IM7/8552 unidirectional pre-impregnated carbon/epoxy tape material. The panels are 16-plies-thick with a nominal cured ply thickness of 0.0049 inch. Cross-ply laminates have stacking sequences of $[0_4/90_4]_S$ and $[0_2/90_2]_{2S}$. And, the quasi-isotropic laminates have stacking sequences of $[+45_2/0_2/45_2/90_2]_s$ and $[+45/0/-45/90]_{2s}$. For the complete experiment set up and details see reference [22].

The specimens have a specification as seen in table II.

Experiment Name	Laminate	Number of Images (Z)
CAR-3-1	Cross-ply	103
CAR-3-2	Cross-ply	102
CAR-5-1	quasi-isotropic	119
CAR-5-2	quasi-isotropic	100

TABLE II: Specimens laminates specifications.

The experiments names do not imply anything but for the purpose of serializing the experiments. The experiments data sets are organized as their own independent stack of CT images with image volume size of $1999 \times 1998 \times Z$, where Z signifies the number of image files as a 3D volumetric information in a sliced fashion, see figure 14.
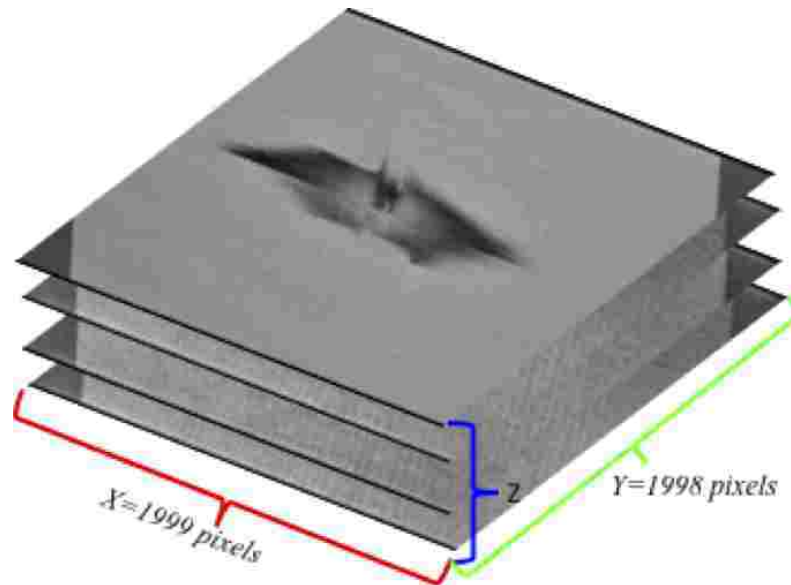
Fig. 14: Experiments sample dimension illustration.

The experiments' damage can be seen from left or front view to give the observer a better understanding of the dameges and correlate the depth of the damages as seen figure 15.
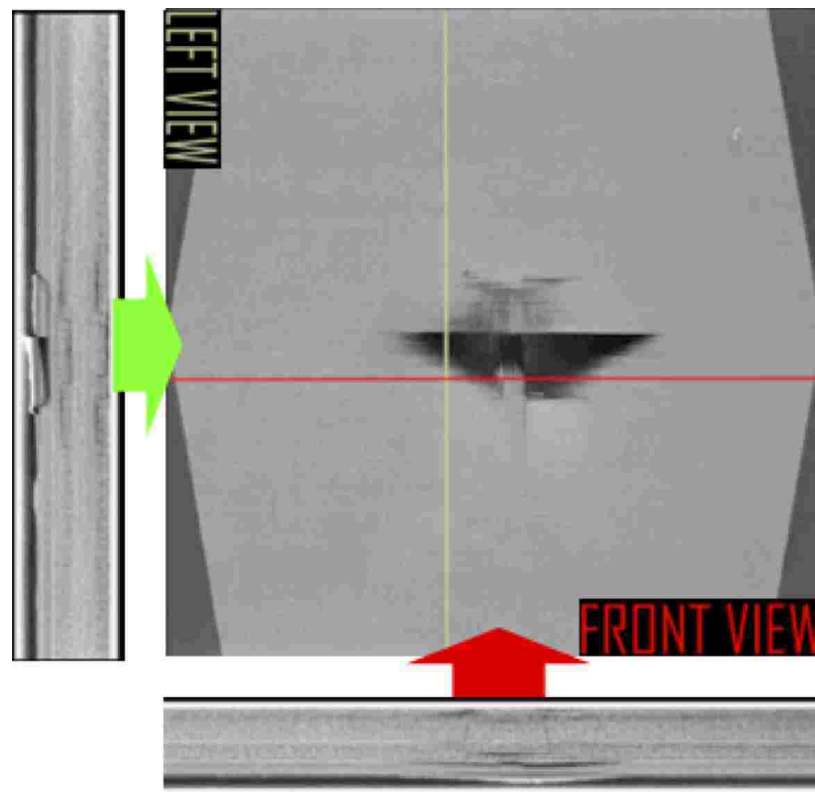
Fig. 15: Front (XZ plane) and left(YZ plane) view of the damage in CAR11C-9-1, the center image is the 21$^{\text{st}}$ image of the experiment.

CHAPTER 3

METHODOLOGY

This chapter covers the innovative approach that was implemented to detect and segment out damage in carbon fiber reinforced polymers using the CT scanned images. This approach starts by preprocessing the CT images and ends with the extraction of the final masking images. The experiment and the acquisition of the images were done by K. Song, F.A. Leone, and C.A. Rose[22].

3.1 Image Preprocessing Stage

The preprocessing of the images starts with enhancing the contrast and the 3D filtering and extracting sub-images for segmentation which is shown in figure 16.

Fig. 16: The three image preprocessing techniques flow diagram.

3.1.1 Contrast Enhancement

To enhance the contrast and compress the 16-bit raw grayscale CT images, the Power-Law (Gamma) transformation was implemented. Mathematically expressed as:

$$I_t = cI_i{}^\gamma \tag{5}$$

Where c and γ are constants. I_i is the input intensity level, which has a range of $[1, 65535]$, 16-bit image, and I_t is the target intensity level, which has a range of $[1, 255]$, 8-bit image. This transformation has two purposes. The first is converting the image from a 16-bit image into an 8-bit image as the input intensity range $[1, 65535]$ maps to $[1, 255]$ of the target intensity range. The second is, as a nonlinear
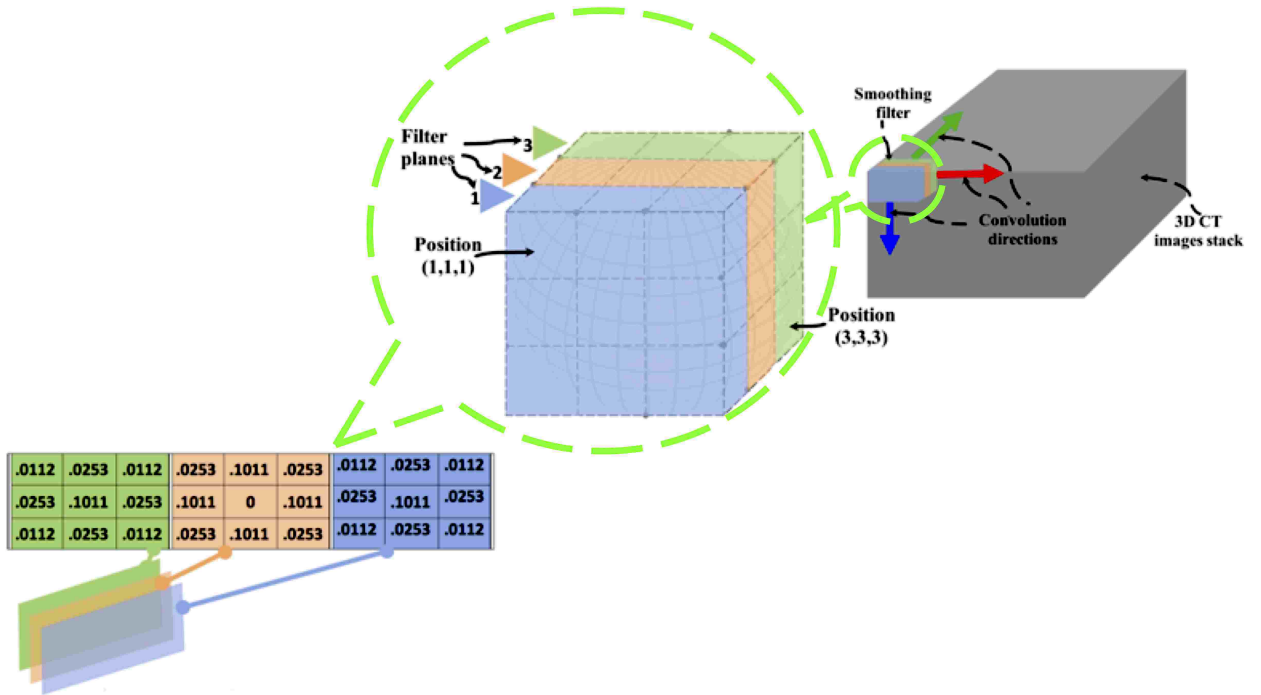
Fig. 17: Illustration of the 3D filtering and filter coefficients values.

transform of the raw image intensity values which acted as an histogram equalizing step. The c and γ values are ≈ 1.0 and ≈ 0.49965, respectively. These values are calculated by solving eq. 5 by substituting the boundary point values of the input and the target intensity levels, which is the reason for the minimum intensity levels for both levels starts at 1 rather than 0, see figure 18- 19.

As seen in figure 18- 20, the contrast of the images is highly variable even if they are from the same experiment representing the same damage at a different depth. By performing the contrast enhancement using the power law, we were able to minimize this variability.

3.1.2 3D Filtering

A 3D smoothing filter that accounts the volumetric aspect of the 3D sliced images was implemented as one of the preprocessing steps. The smoothing of the voxels; here voxels and pixels mean the same except we prefer to call the pixels as voxels to imply the pixels are now considered in a 3D spatial space rather than in their normal 2D spatial space.
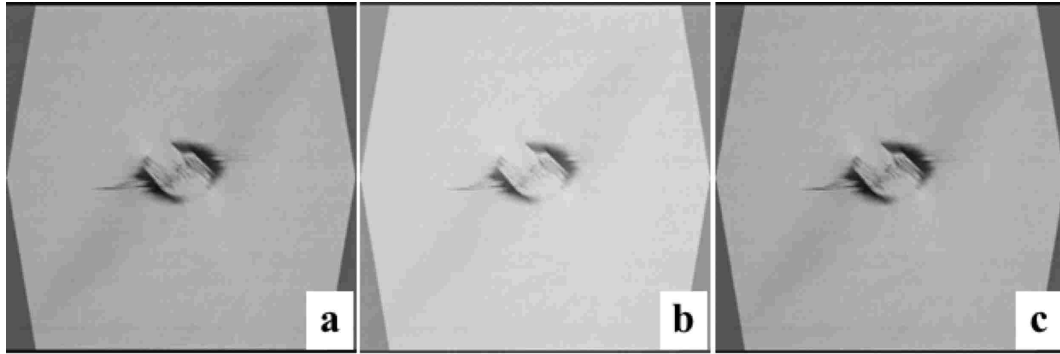
Fig. 18: Experiment CAR-5-1, image 39. (a) raw image, (b) contrast enhanced, gamma transformed, and (c) 3D filter smoothed image.
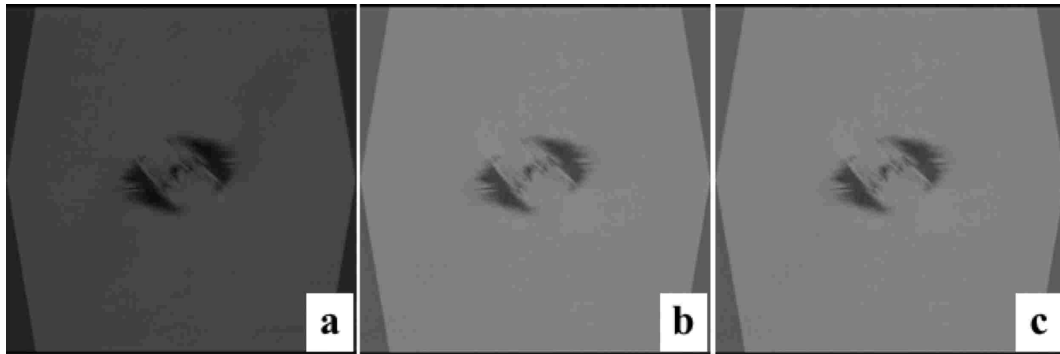
Fig. 19: Experiment CAR-5-1, image 4. (a) raw image, (b) contrast enhanced, gamma transformed, and (c) 3D filter smoothed image.

The implemented 3D smoothing filter is $3 \times 3 \times 3$ in size. The filter voxel values were calculated as the inverse square-root of the distance from center, considering the $3 \times 3 \times 3$ filter as a sphere and pixels position as a distance unit, seen in figure 17, which became the weighting average values and assigned to each element in according to their 3D spatial position. The sum of the filter is normalized to one, to be exact .9998, and the center voxel has a weighting constant value zero as it is the voxel that will be replaced when the filter is applied centering that voxel. Figure 17 shows the filtering directions on the 3D CT images stack and the arrangement of the filters and the assigned values for the filter coefficients.
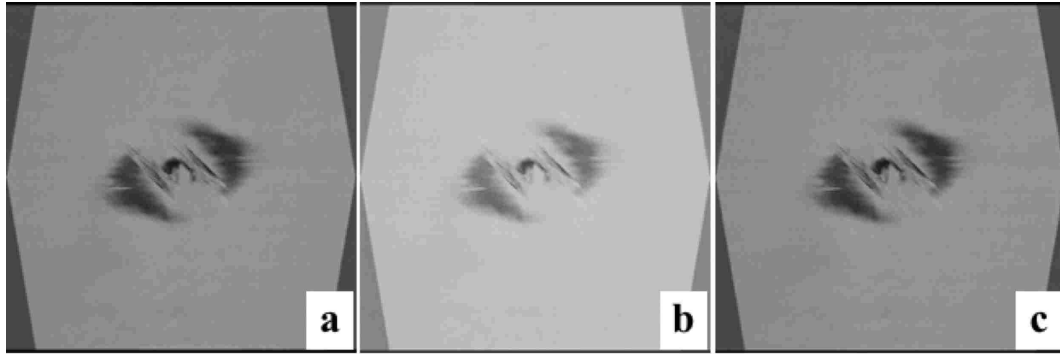
Fig. 20: Experiment CAR-5-1, image 43. (a) raw image, (b) contrast enhanced, gamma transformed, and (c) 3D filter smoothed image.

3.1.3 Sub-Images Extraction

Lets start by previewing figure 21 which has two areas with a damaged and non-damaged pixel intensities. This is one of the major challenges which a SME encounters during segmentation as sometimes the material structure itself resembles a damage while observing from close-in but clearly not a damage from a distant perspective. This problem is alleviated by considering three views of the same area at different windowing sizes which we call it View 1, View 2, and View 3, see figure 22. As it can be seen that it is easier to name the monument as the Washington monument in View 3, however View 1 gives a best localization of the monument. Further more, View 2 is a balanced representation of the localization and identity of the monument due to the surrounding ground structure of the monument. Using the above analogy, let's translate the concept to the CT scanned images. Firstly, the windowing size is increased twice from one view to another view length and width wise. Thus, for a 32×32 sized View 1; View 2 would center View 1 but has a size of 64×64 and View 3 includes both at the center with windowing size of 128×128.

For illustrating the idea behind the innovative sub-image extraction, a sub-image sample's size of $32 \times 32 \times 9$ is used. The 32×32 dimension of the sub-image represents the spatial representation of the sub-image which is the same as the size as View 1. The third dimension depth of nine represents the sub-image's channels, which we discussed how each of the channels are generated in the later part of this section.

The windowing and the generation of the nine channels for each windowing is
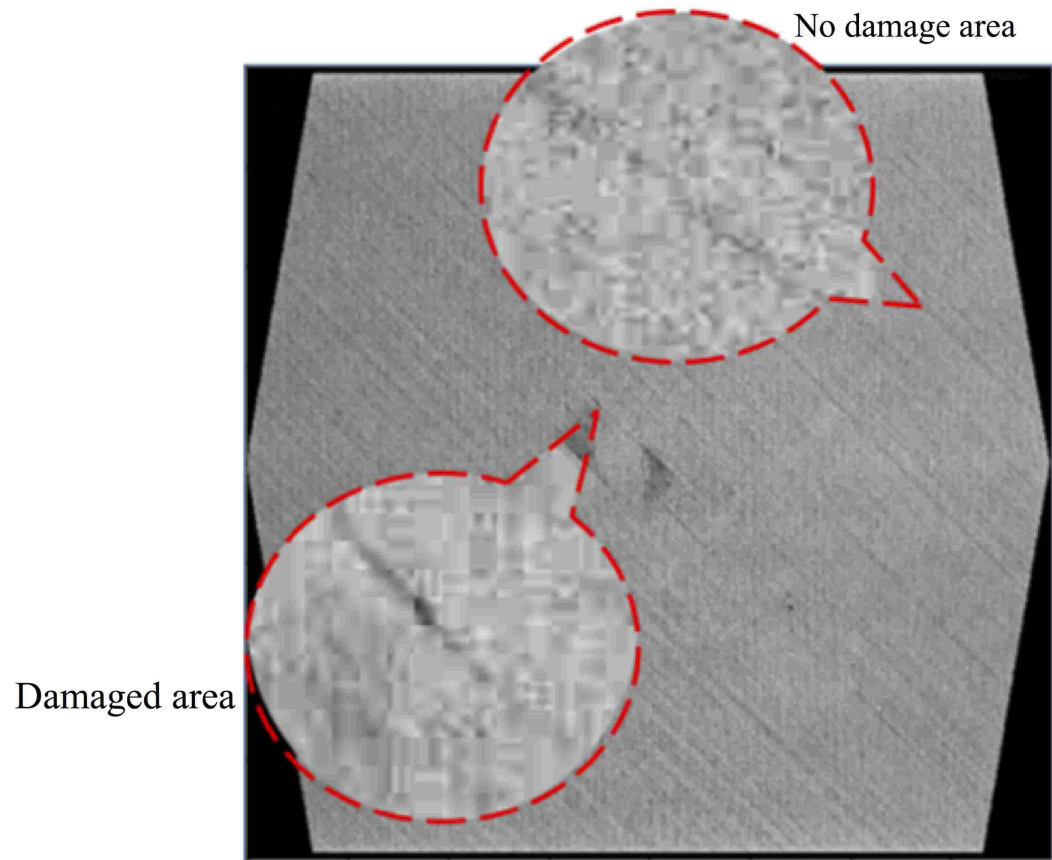
Fig. 21: Illustration of one of the major challenges during magnification of ROI to identify damage within an area.
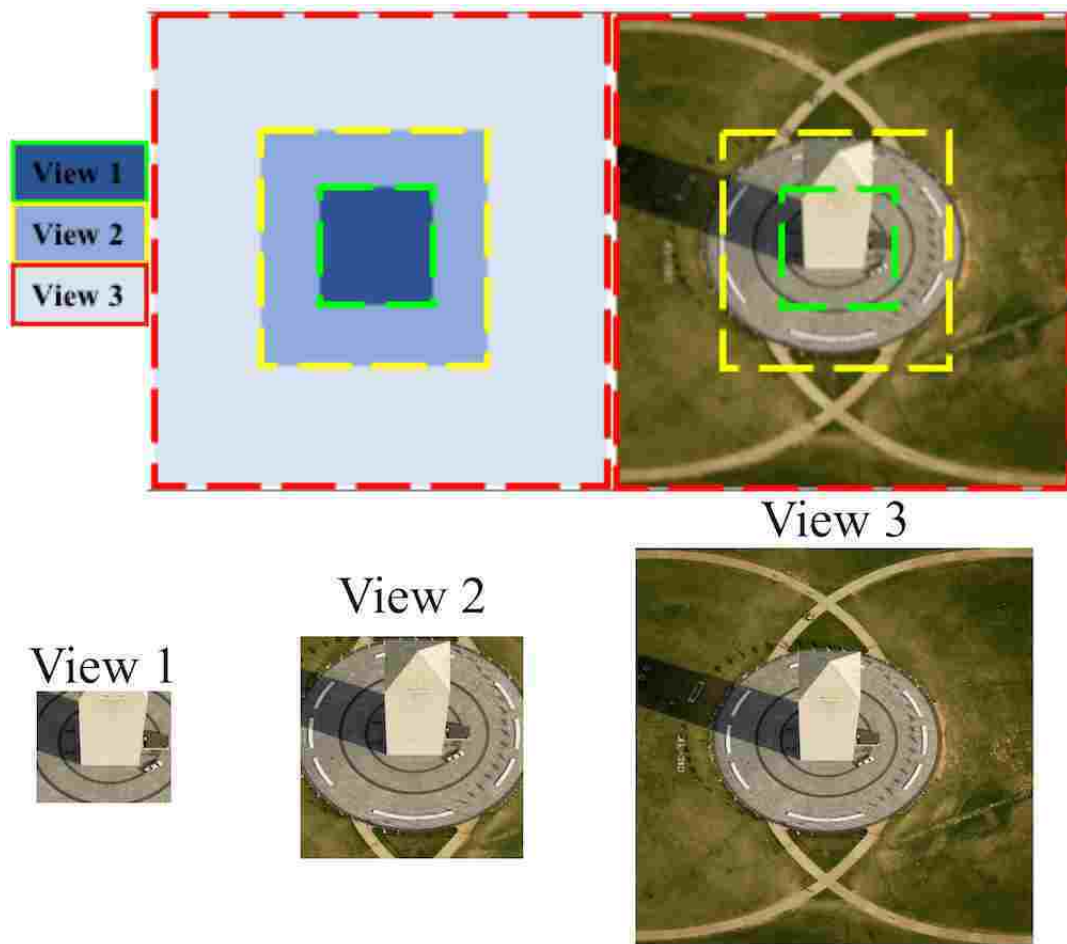
Fig. 22: Illustration of windowing and extraction of View 1, View 2, and View 3 using Washington Monument[23] .
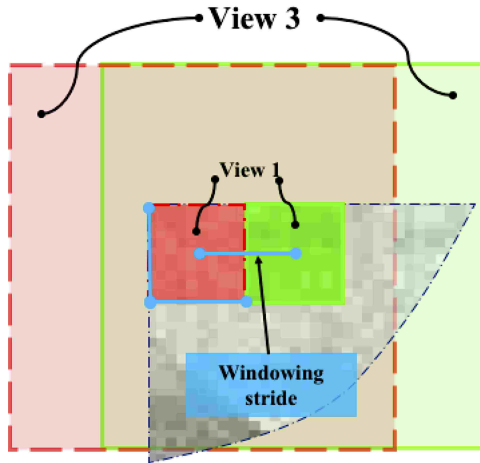
Fig. 23: Illustration of sampling View 1, View 2, and View 3 for neighboring subsampling windows.

performed throughout the image with a windowing stride of View 1 size with no overlap of the different View 1s, shown in figure 23. But, Views 2 and 3 overlap with the neighboring views as the stride size is $\times 2$ and $\times 4$ less than View 2 and View 3, respectively.

Remember for the example above, View 1 has a windowing size of 32×32, View 2 has a size of 64×64 and View 3 has a size of 128×128. These views are different in size, furthermore View 2 and View 3 are 8 and 16 times the size of View 1, respectively. Thus, we need to come up with some way to combine these views and be able to feed it to a CNN model as an input without losing relevant or adding irrelevant information other than the information from the image under consideration.

To do so, we develop an approach that utilizes the 2D wavelet transform unique separability of the directional coefficients and its downsampling steps. Enabling the 9-channel sub-images to represent a three point view perspectives of the windowed image which mimics the zooming-in effect to localize the damage while keeping the neighboring pixels information to give us a better perspective of the area under consideration. This is exactly what a SME would do to identify and classify region of interest and whether it has damage or not.

The major decision factor for the views' size to be a power of two is due to explicit downsampling($\times 2$) that occurs during each level transform when applying the HDWT, which resulted the approximation and details coefficients to have the
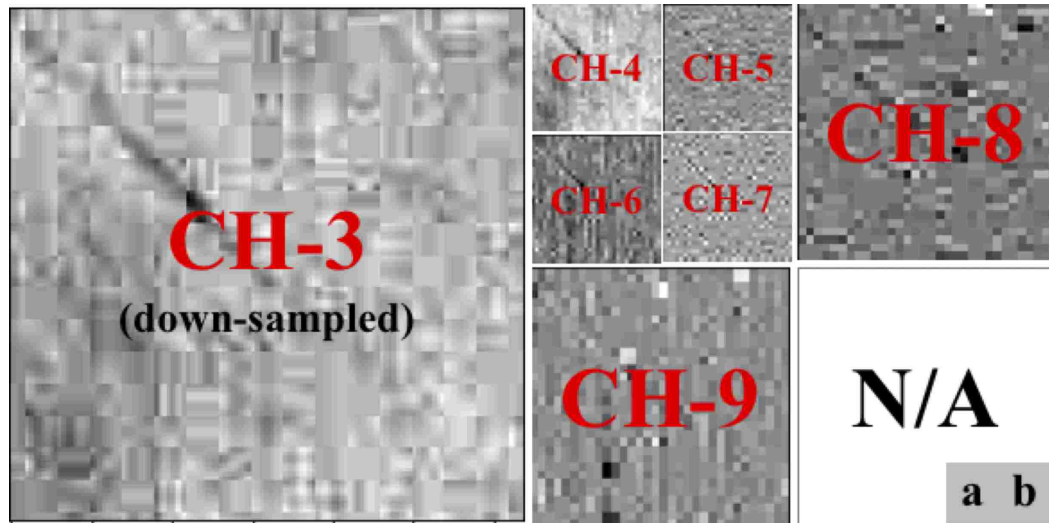
Fig. 24: Detailed illustration of the wavelet transformed coefficients for View 3 and their respective channel place.

same size as View 1 after performing second-level HDWT on View 3 and ×2 the size of View 1 after the first-level transform.

For the above examples, the three views then combine to make the nine channels as follows:

1. **Channel 1**: consists of View 1 pixel only.

2. **Channel 2**: consists of View 2 (64×64) downsampled ×2, which become 32×32, pixels values only.

3. **Channel 3**: consists of View 3 (128×128) downsampled ×4, which become 32×32, pixels values only. **Note**: refer figure 24 to see how the sub-image channels 4 to 9 generated using wavelet transform.

4. **Channel 4**: consists of the second-level Haar Discrete Wavelet Transform (HDWT) approximation coefficients, 32×32, of View 3.

5. **Channel 5**: consists of the second-level HDWT horizontal details coefficients, 32×32, of View 3.

6. **Channel 6**: consists of the second-level HDWT vertical details coefficients, 32×32, of View 3.

7. **Channel 7**: consists of the second-level HDWT diagonal details coefficients, 32×32, of View 3.

8. **Channel 8**: consists of the first-level HDWT horizontal downsampled $\times 2$ details coefficients, 32×32, of View 3.

9. **Channel 9**: consists of the first-level HDWT vertical downsampled $\times 2$ details coefficients, 32×32, of View 3.

3.2 CNN Models Architecture

There are three implemented CNN model architectures collectively named *Focused, Near and Distant (**FiND**)* models. The major difference between the three models are the sub-image they take at their input layer. The difference in their inputs and architectures are to account for various types and levels of noise as well as to incorporate different levels of perspectives while observing the CT images at different levels of views.

The Focused model takes $2 \times 2 \times 9$ sub-images at the input layer and predicts the sub-image as damaged ("1") or non-damaged ("0") sub-image. The predicted output labels will be set on the 2×2 subsampling window which is the same as View 1 of the sub-images. The primary purpose of the focused model is to pick-up fine cracks which will be harder to do at a higher sub-image sampling size. The size of View 1, View 2, and View 3 for these models are 2×2, 4×4, and 8×8, respectively. The architecture of the CNN model is given as a table in table III.

The Near model takes $4 \times 4 \times 9$ sub-images at the input layer and predicts the sub-image as damaged ("1") or non-damaged ("0"). The predicted output labels will be set on the 4×4 subsampling window which is the same as View 1 of the sub-images. The purpose of this model is to pick-up major cracks and the fine edge of delamination. The size of View 1, View 2, and View 3 for these models are 4×4, 8×8, and 16×16, respectively. The architecture of the Near CNN model is given in table IV. Most importantly, it is the balance between the Focused and the Distant models.
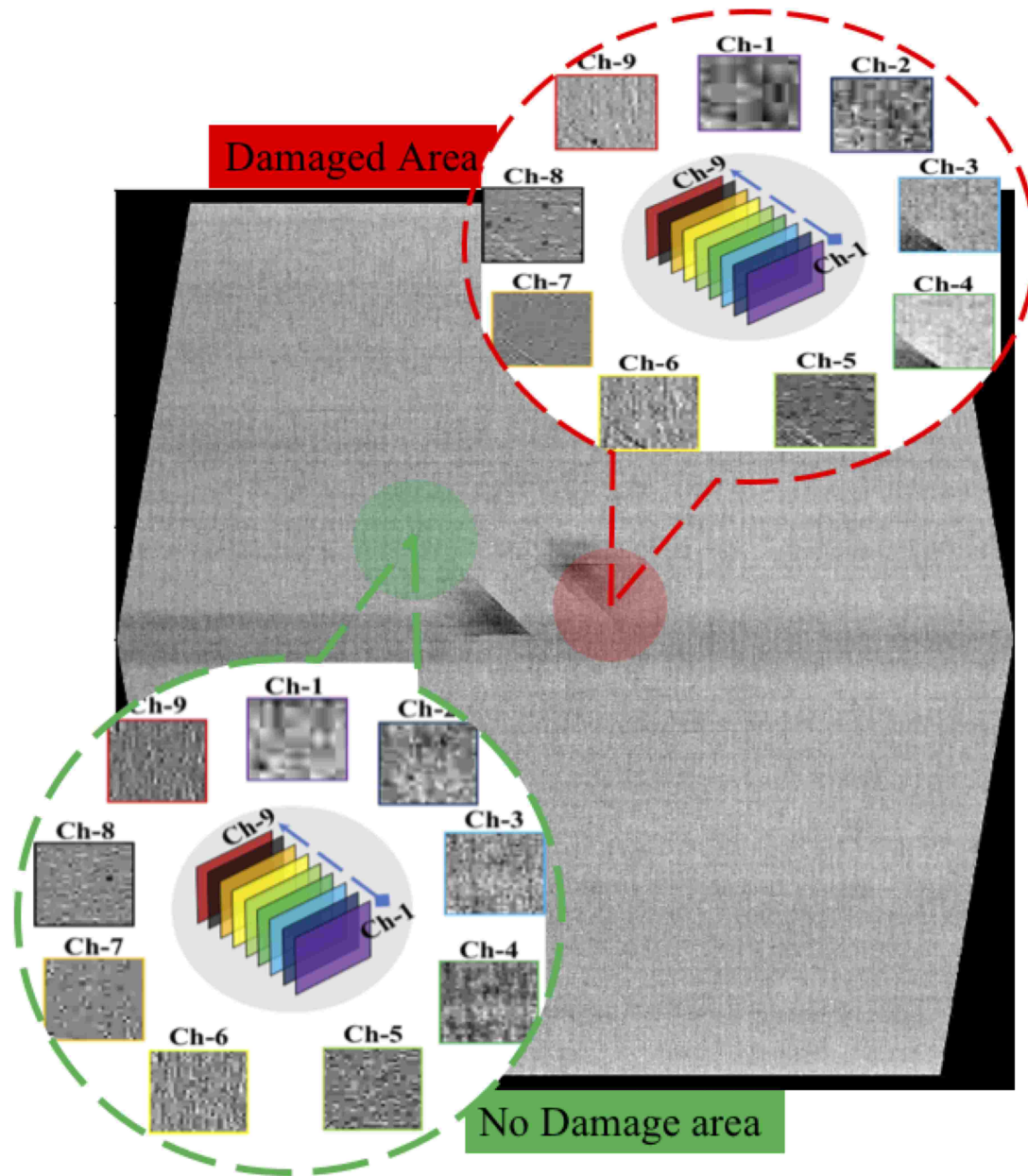
Fig. 25: Illustration of no damage(green), and damaged(red) areas from normal and zoom-in perspective.

Layer #	Layer Type	Input Size	Kernel Size	Output Size
1	Input	(2,2,9)	-	(2,2,9)
2	2D Conv	(2,2,9)	36 (1,1)	(2,2,36)
3	ReLu	(2,2,36)	-	(2,2,36)
4	Max Pool	(2,2,36)	(2,2)	(1,1,36)
5	Flatten	(1,1,36)	-	(36)
6	Dense	(36)	-	(36)
7	ReLu	(36)	-	(36)
8	Dropout	(36)	50%	(36)
9	Dense	(36)	-	(1)
10	Sigmoid	(1)	-	(1)
11	Output	(1)	-	(1)

TABLE III: The Focused model architecture.

Layer #	Layer Type	Input Size	Kernel Size	Output Size
1	Input	(4,4,9)	-	(4,4,9)
2	2D Conv	(4,4,9)	64 (2,2)	(3,3,64)
3	ReLu	(3,3,64)	-	(3,3,64)
4	Max Pool	(3,3,64)	(2,2)	(1,1,64)
5	Flatten	(1,1,64)	-	(64)
6	Dense	(64)	-	(64)
7	ReLu	(64)	-	(64)
8	Dropout	(64)	50%	(64)
9	Dense	(64)	-	(1)
10	Sigmoid	(1)	-	(1)
11	Output	(1)	-	(1)

TABLE IV: The Near model architecture.

The Distant model takes $8 \times 8 \times 9$ sub-images at the input layer and predicts the sub-image as damaged ("1") or non-damaged ("0"). The predicted output labels are set in the 8×8 subsampling window as final masking output for the model. The

purpose of this model is to pick-up delamination by minimizing localized noises as it considers a larger perspective of the area under observation. The size of View 1, View 2, and View 3 for these models are 8×8, 16×16, and 32×32, respectively. The architecture of the model is given in table V.

Layer #	Layer Type	Input Size	Kernel Size	Output Size
1	Input	(8,8,9)	-	(8,8,9)
2	2D Conv	(8,8,9)	64 (3,3)	(6,6,64)
3	ReLu	(6,6,64)	-	(6,6,64)
4	Max Pool	(6,6,64)	(2,2)	(3,3,64)
5	2D Conv	(3,3,64)	128 (2,2)	(2,2,128)
6	ReLu	(2,2,128)	-	(2,2,128)
7	Max Pool	(2,2,128)	(2,2)	(1,1, 128)
8	Flatten	(1,1, 128)	-	(128)
9	Dense	(128)	-	(64)
10	ReLu	(64)	-	(64)
11	Dropout	(64)	50%	(64)
12	Dense	(64)	-	(1)
13	Sigmoid	(1)	-	(1)
14	Output	(1)	-	(1)

TABLE V: The Distant model architecture.

3.3 Generating Data set for Training

As discussed in sec 3.2, there are three distinct CNN models implemented which we named Focused, Near, and Distant models. Furthermore, each model's input size and model architecture is different. Thus, we need to generate three distinct sets of training, validation, and test data sets. In addition, there is one more difference between the models which is how a sub-image is classified as damaged("1") and non-damaged("0") during training the models. This labeling of sub-images is based on their *Damage Threshold Pixels (DTP)* values set for each model.

The damage threshold pixels (DTP) are a collection of pixels in a squared box around the center of View 1 which have a corresponding pixel value of one in the ground truth masking image, refer figure 26. Normally, the DTP is given as a scalar
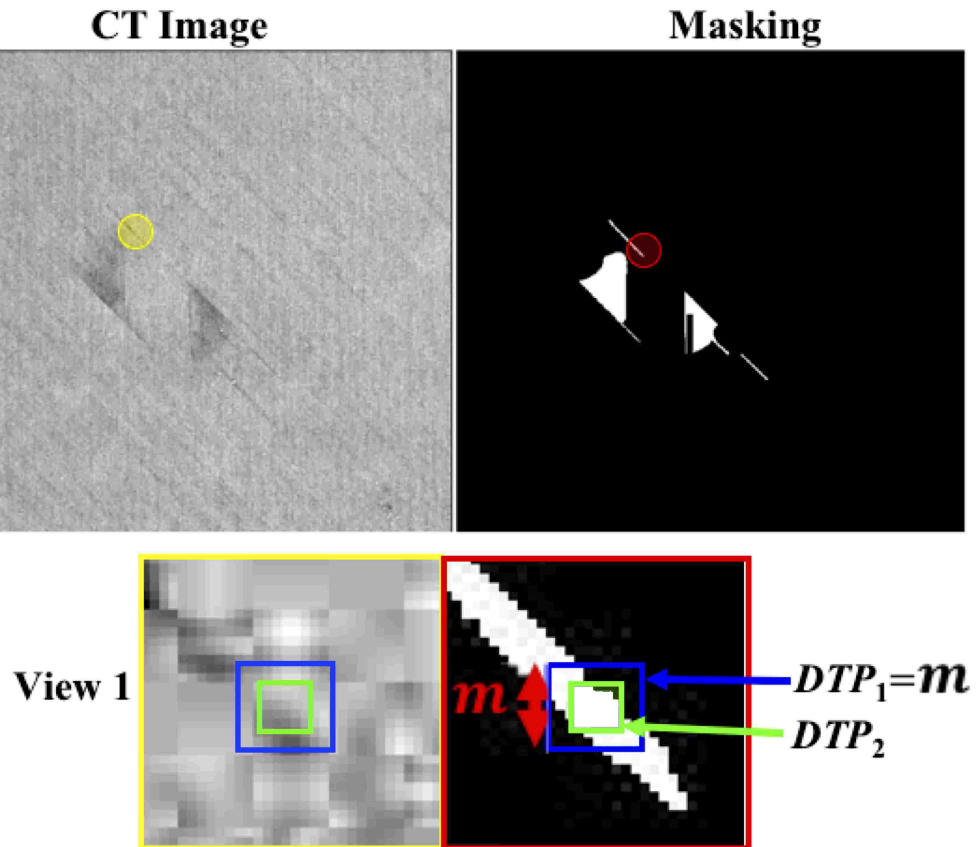
Fig. 26: Illustration of how damage threshold pixels are localized and extracted.

which represent the dimensions of the square box.

A sub-image is to be considered a damaged sub-image ("1"), the designated DTP pixels all need to have a corresponding pixel value of one in the masking image otherwise the sub-image is labeled as no-damage ("0"). As seen in figure 26, the threshold value of $DTP_1 > DTP_2$ which makes DTP_1 less susceptible to noisy pixels but misses small cracks where as DTP_2 is great for finer details but fails to reject noisy pixels.

Model Name	Sub-image Size	Damged Threshold Pixels(DTP)	# Samples					
			Training (67.5%)		Validation (22.5%)		Test (10%)	
			"0"	"1"	"0"	"1"	"0"	"1"
Focused	(2x2x9)	1	6750	6750	2250	2250	1000	1000
Near	(4x4x9)	2	3375	3375	1125	1125	500	500
Distant	(8x8x9)	4	3375	3375	1125	1125	500	500

TABLE VI: Data set samples and class distribution.

CHAPTER 4

RESULTS

As discussed in section 3.1.3, extraction of the sub-images and their class labels are not based on a pixel-by-pixel value, rather the developed Damage Threshold Pixels (DTP) was used to label the sub-images. Thus, to assess the performance of the models, the generated datasets were divided into training, validation, and test data sets. In addition, a confusion matrix table and Receiver Operating Characteristics (ROC) were implemented to assess the trained models performance. However, before discussing confusion matrix and ROC, which T. Fawcett[24] presented well in his 2005 article, let's assess the training progress of the trained models.

4.1 FiND Models Training Performance

During the training, the models' accuracy, loss, and Mean Absolute Error(mae) were monitored 27- 29. At the beginning of the models training runs, all the monitored metrics were unstable. However, as the training progressed, the learning rate was set to decay, to stabilize the loss function weights, and the model to convergence to the approximated solution. This resulted in a steady increase in accuracy will minimizing the loss function.
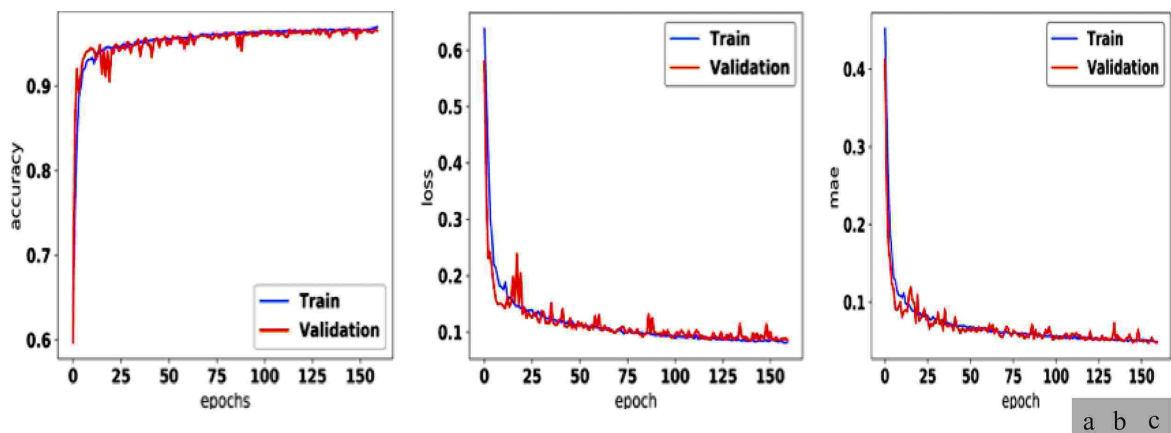

Fig. 27: Focused model training and validation data set (a) accuracy, (b) loss, and (c) mean absolute error during model training.
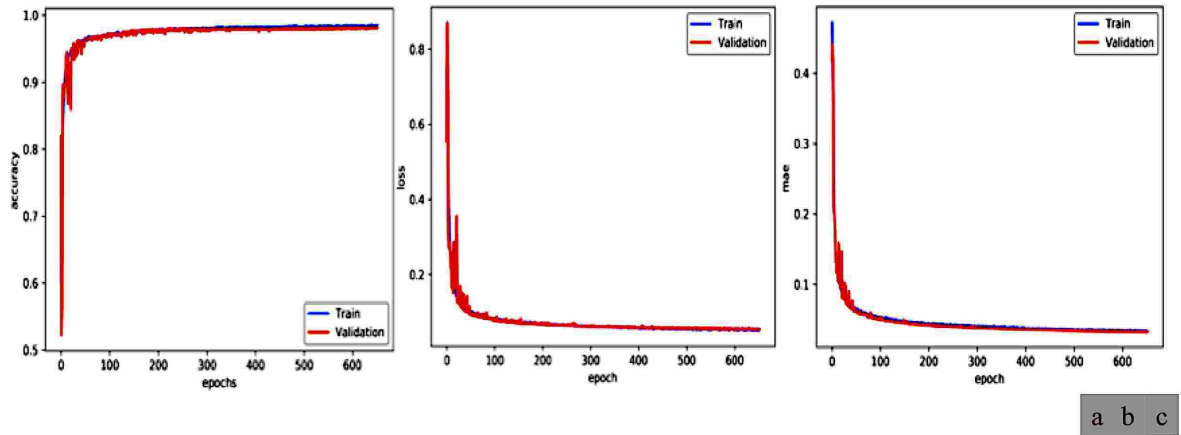
Fig. 28: Near model training and validation data set (a) accuracy, (b) loss, and (c) mean absolute error during model training.
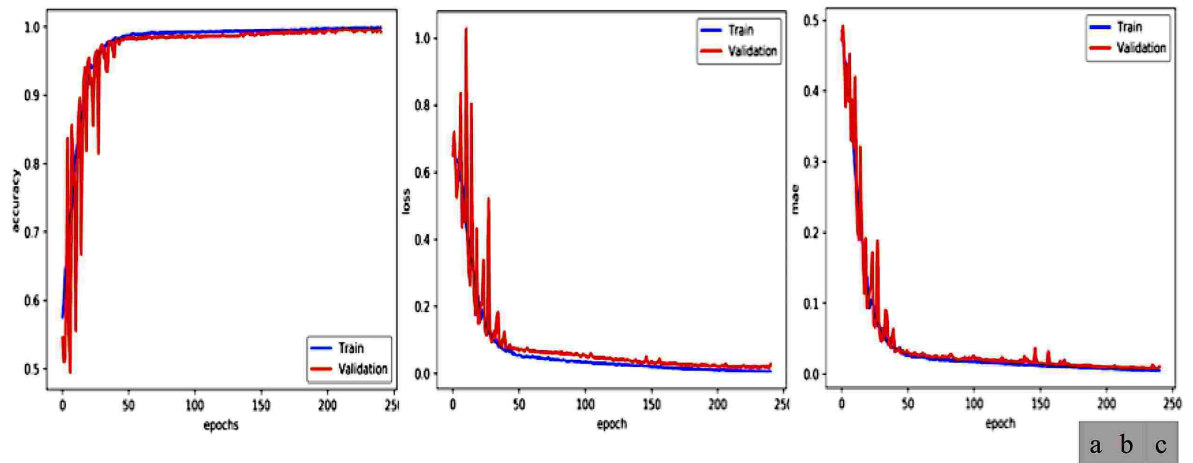

Fig. 29: Distant model training and validation data set (a) accuracy, (b) loss, and (c) mean absolute error during model training.

In our case, we have two discrete classes. Thus, a sub-image class prediction would have four possible outcomes, $i.e.$[24]:

1. **True Positive (TP)**: If the sub-image is "1" and classified as "1".

2. **False Negative(FN)**: If the sub-image is "1" but classified as "0".

3. **True Negative(TN)**: If the sub-image is "0" and classified as "0".

4. **False Positive(FP)**: if the sub-image is "0" and classified as "1".

By classifying the predicted class labels for the test sub-image data sets into TP, FN, TN, and FP a two-by-two matrix, also named as confusion matrix (contingency table) as seen in figure 30 is generated. In addition, using the above layout one can now calculate true positive rate ($tp\ rate$) and false positive rate ($fp\ rate$)[24]; which are considered for ROC.

ROC is a 2D graph in which the $tp\ rate$ is plotted on the vertical axis and the $fp\ rate$ is plotted on the horizontal axis. The ROC graph indicates the tradeoffs between TP(benefits) and FP(costs)[24]. And, the $tp\ rate$ and $fp\ rate$ are calculated as:

$$tp\ rate \approx \frac{Positives\ correctly\ classified}{Total\ positives} \tag{6}$$

$$fp\ rate \approx \frac{Negatives\ incorrectly\ classified}{Total\ negatives} \tag{7}$$

According to T. Fawcett[24], for a discrete classifier the points (0,0), (0,1), and (1,1) in figure 31 are important points. But, neural networks predict instances to a degree to which they represent a class, by assigning a probability score, $i.e.$ a numeric value between $[0, 1]$ as to an instance is a member of a class. Additionally, one point in ROC space is better than another if the $tp\ rate$ is higher, the $fp\ rate$ is lower, or both which the trained models exhibit.

The point (0,0) represents a classifier which neither predicts false positive errors nor gains true positives, which ultimately issue no positive classification. The point $(1, 1)$ represents a classifier which unconditionally issues positive classifications. Whereas, the point $(0, 1)$ represents perfect classification.

But, to compare classifiers reducing the ROC performance to a single scalar value representing the expected performance is ideal. To do so, Area Under the ROC
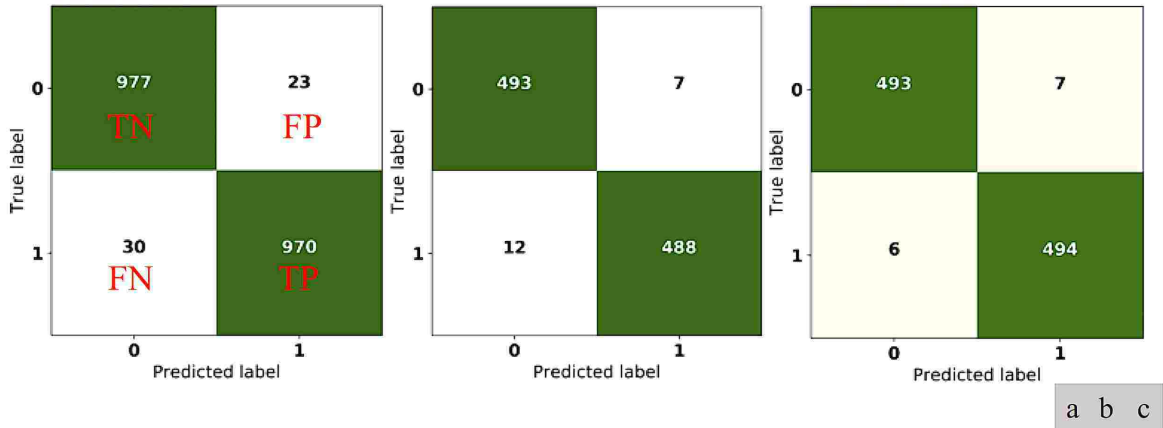
Fig. 30: Confusion matrices for (a) focused, (b) near, and (c) distant model test data sets with 0.5 threshold for class identification.
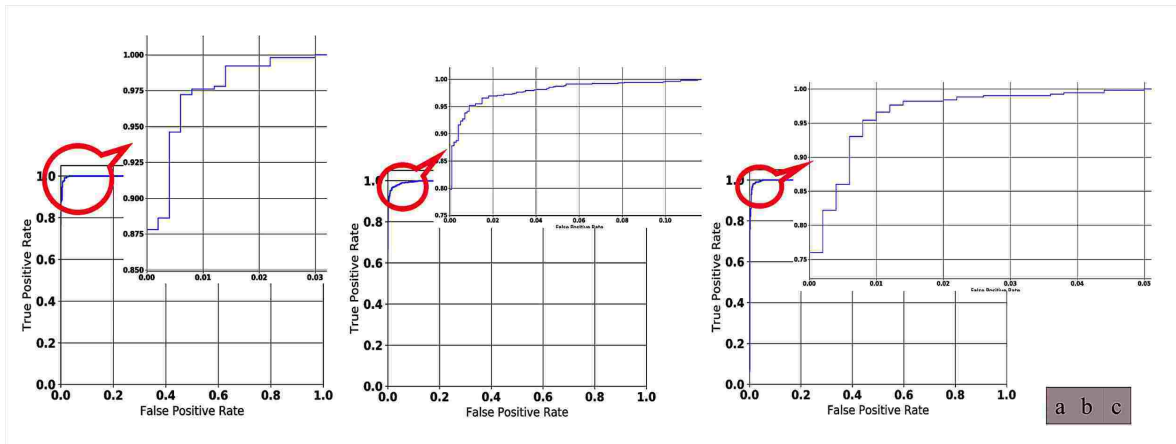
Fig. 31: ROC for (a) focused, (b) near, and (c) distant models. The points are calculated using eq. 6 and 7 by substituting the results from the resulted confusion matrices as in figure 30.

(AUC) is calculated. AUC is equivalent to a probability that a classifier will rank a randomly chosen positive instance higher than a randomly chosen negative instance which is equal to the area of a unit square[24]. AUC value is between 0 and 1, however a model better than randomly guessing should have a value more than 0.5 and a perfect model would have 1. For our case, the Focused model has 0.9991, the Near model has 0.9974 and the Distant model has 0.9982 AUC.

4.2 Segmentation Performance of FiND models

The results presented under this section are the segmentation of the CT images using the three FiND models, shown from figure 32-37. As it shows in the figures, the Focus model was able to pick every detail of the damage but also the false positives(noise) that were eventually picked up as damage. Whereas, the Distant model was able to pick up the delamination regions effectively while missing the cracks. The Near model picked up both the cracks and the delamination damages in the composite material.

The other major difference is the smoothness of the edges on the boarder lines as well as the damage edges. This is due to the fact of each model's prediction sampling size. The Focused model has a smaller prediction windowing size of $2 \times 2$ whereas the Distant model has a prediction of size of 8×8 which incurs rougher edges than the Focused model.

Figure 34 and 37 shows how the three predictions can be combined to result a colored segmentation image with RGB channels with Red, Green, and Blue channels represented by Focused, Near, and Distant Models, respectively. As the distant model does not pick up cracks, one quickly sees the segmented cracks in red or greenish-yellow color when the crack is located in isolation to the delamination. And, the delamination is represented as solid white. This way, the noise effect is minimized as the three predictions contribute to the resulting segmentation.

The other thing to observe in figure 34(a) and 37(a) is the models' prediction at the boarder of the images. At the boarder, the color changes from red to yellow then white. This is due to the fact that the subsampling starting and ending point for the three models are different as they have different windowing size for View 3. As the windowing size of View 3 for Focused model is 8×8 while for the Near model is 16×16 and Distant model is 32×32. Thus, instead of padding and increasing computation, the starting and end points are half of the size of the respective View 3. *i.e.*, if the origin is at (0,0) then the Focused model center starts at (3,3), the Near model start at (7,7) and the distant model at (15,15).

Figure 34 and 37 with their respective (a), (b), and (c) show the segmentation of the CT images with the predicted masking images using the FiND models. The distant model gives the overall location of the damage while the Focused and Near models follow the damage structure and tighter to the damage boarder specially for cracks. The delamination is best segmented with the distant model.
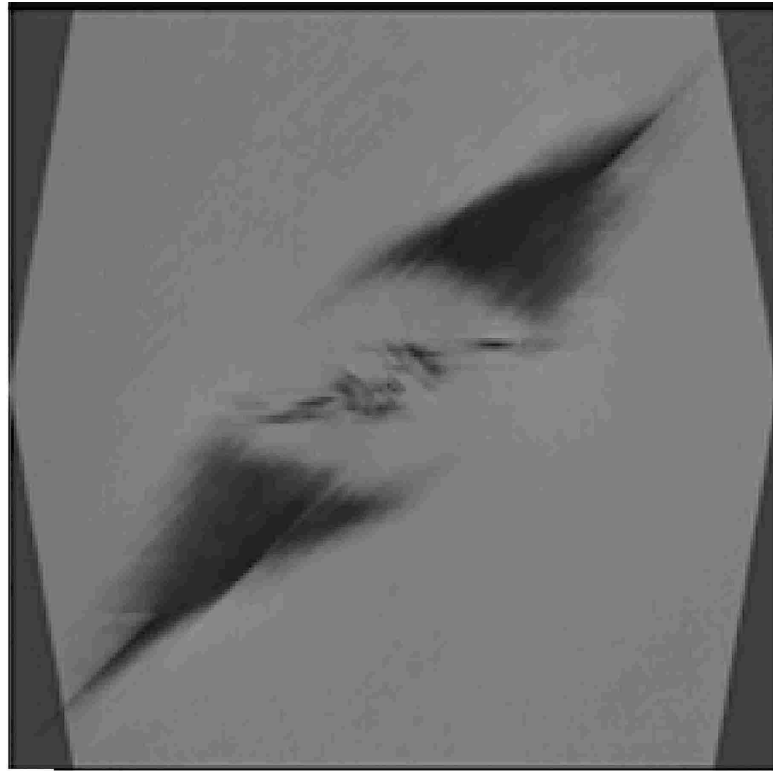
Fig. 32: (a) Preprocessed raw CT image and (b) Masking predicted using Focused.

Fig. 33: Figure 32(a) image's masking predicted using (a) Near and (b) Distant models.

Fig. 34: (a) Figure 32(b), 33(a), and 33(b) are combined to one colored image using RGB representation which are assigned as Focused(R channel), Near(Green channel), and Distant(Blue channel). And, (b) to (d) are segmentation of figure 32(a) using Focused, Near, and Distant models, respectively.

Fig. 35: (a) Preprocessed raw CT image and (b) Masking predicted using Focused.
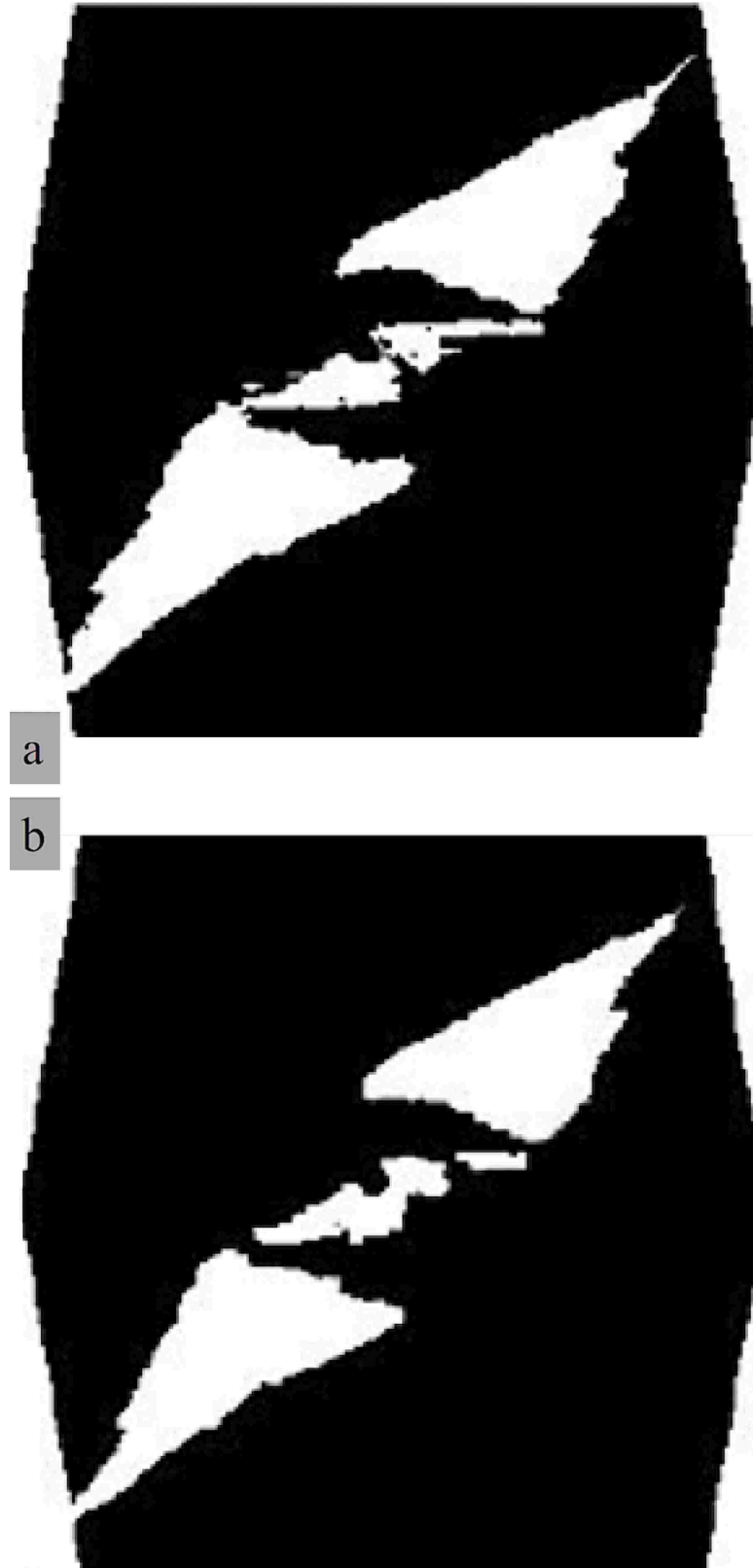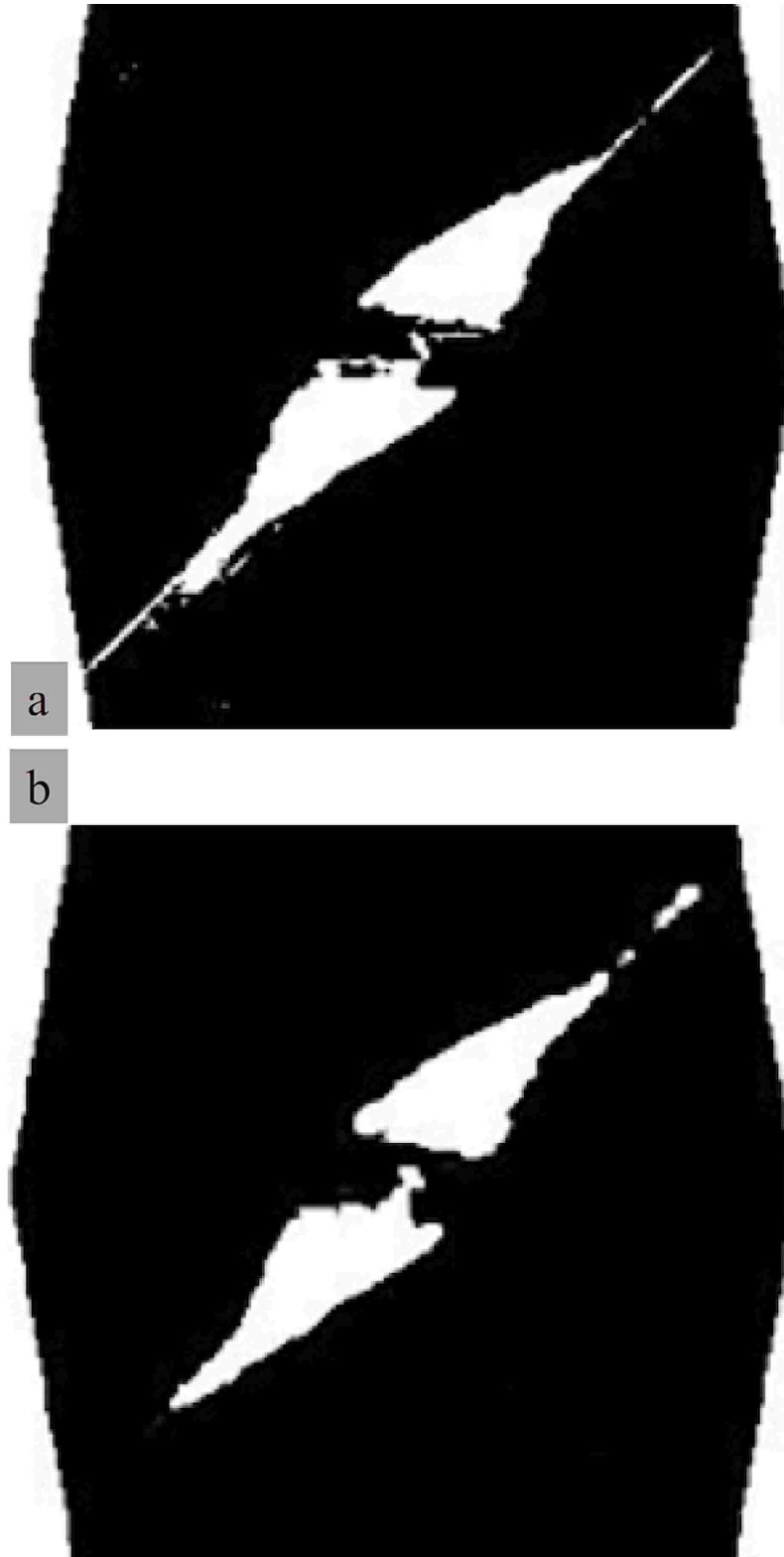
Fig. 36: Figure 32(a) image's masking predicted using (a) Near and (b) Distant models.
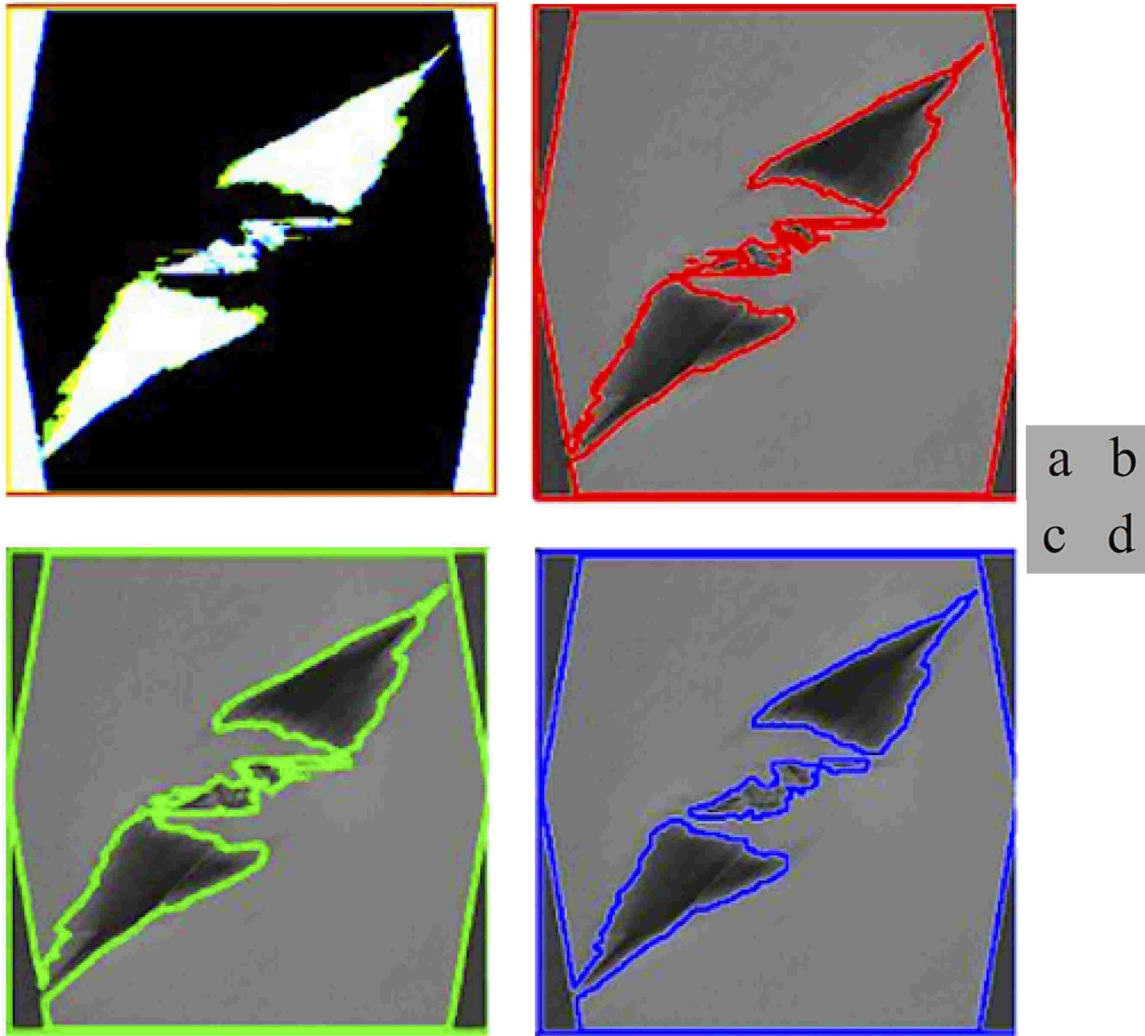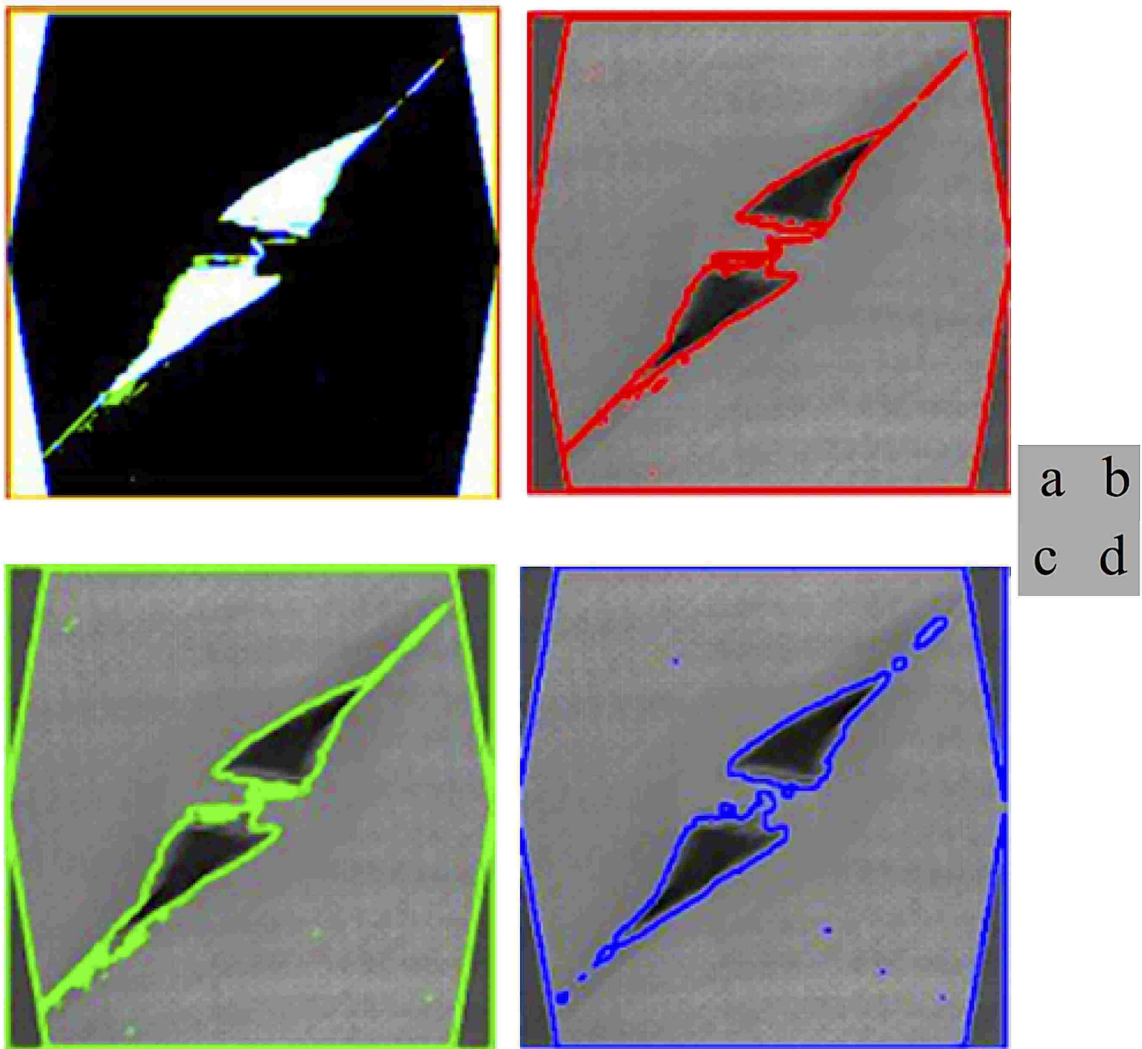
Fig. 37: (a) Figure 35(b), 36(a), and 36(b) are combined to one colored image using RGB representation which are assigned as Focused(R channel), Near(Green channel), and Distant(Blue channel). And, (b) to (d) are segmentation of figure 32(a) using Focused, Near, and Distant models, respectively.
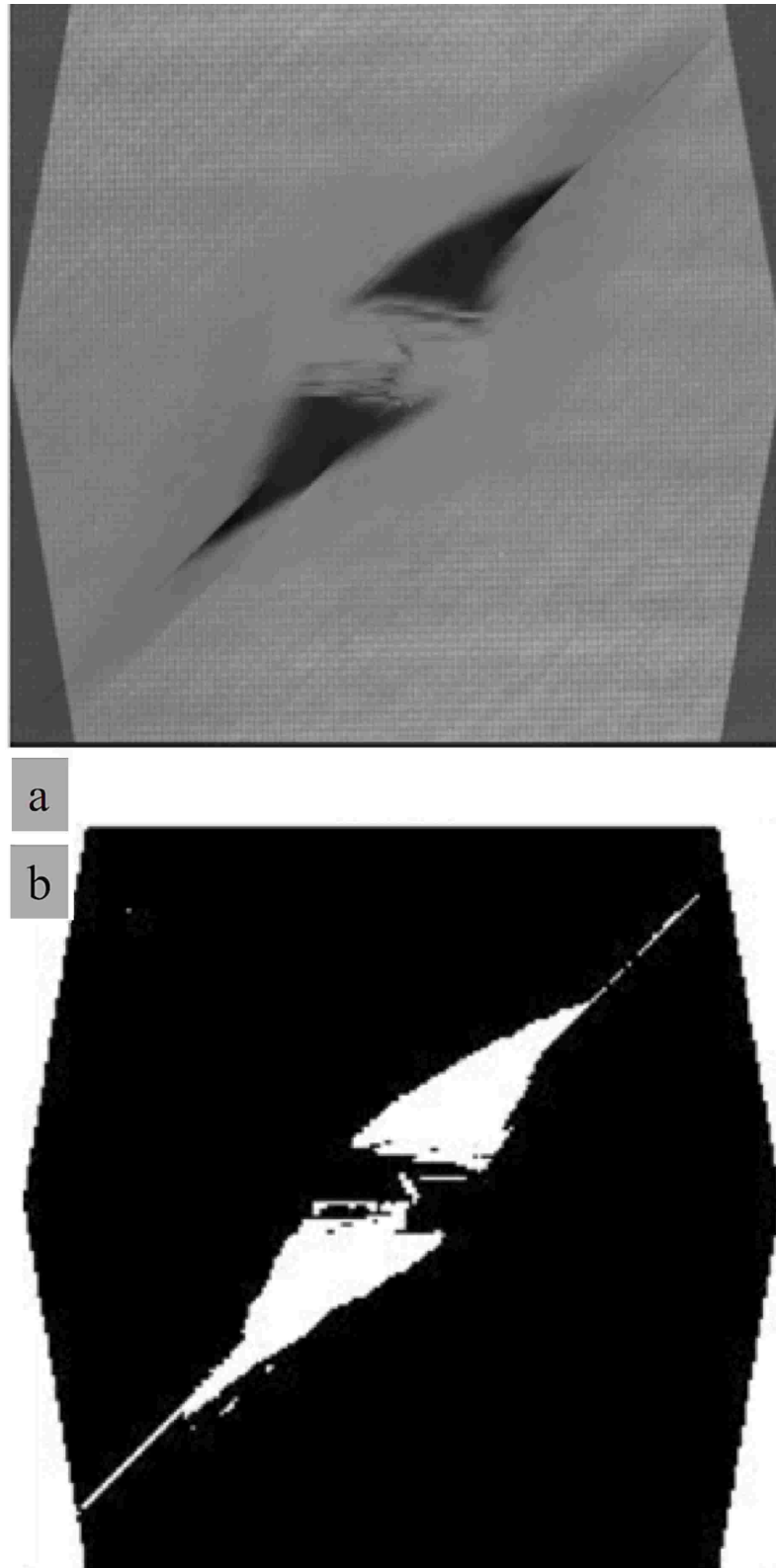
Figure 38(b) shows results from a method that was developed by D. Sammons, L. Chen and R. Milletich[25] using CNN architecture and figure 38(c)-(d) shows the FiND models' predictions. The results predicted by the FiND models depict the structural damage that is observed in the CT image but fail to predict all the damage representing pixels. This true negative rate is more pronounced if the CT image is not preprocessed to have a better contrast, see figure 39.

In this perspective, the contrast of the image is important but enhancing the contrast of an image does not take a lot of time compared to segmenting the actual damage which in the first place was consuming the SME time in locating and identifying the damages in the composite material. In addition, if the intention is to segment out delamination damage only, then it is best to use the distant model rather than the Focused and Near models.

Fig. 38: (a) Preprocessed CT image. Maskings predicted using (b) Focused, (c) Near, and (d) Distant model.

Fig. 39: (a) Simulated CT image with delamination[15]. Maskings predicted using (b) Focused, (c) Near, and (d) Distant model. (e) Contrast enhanced image of (a). From (f) to (h) are prediction of (e) using the Focused, Near, and Distant models, respectively.

CHAPTER 5

CONCLUSIONS

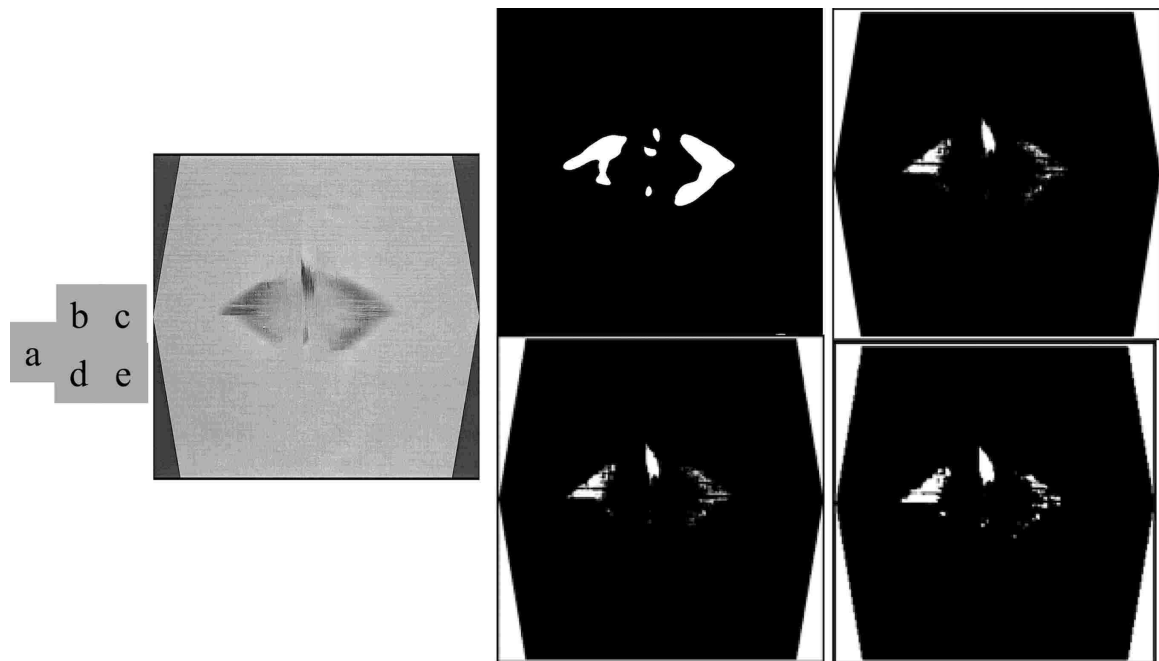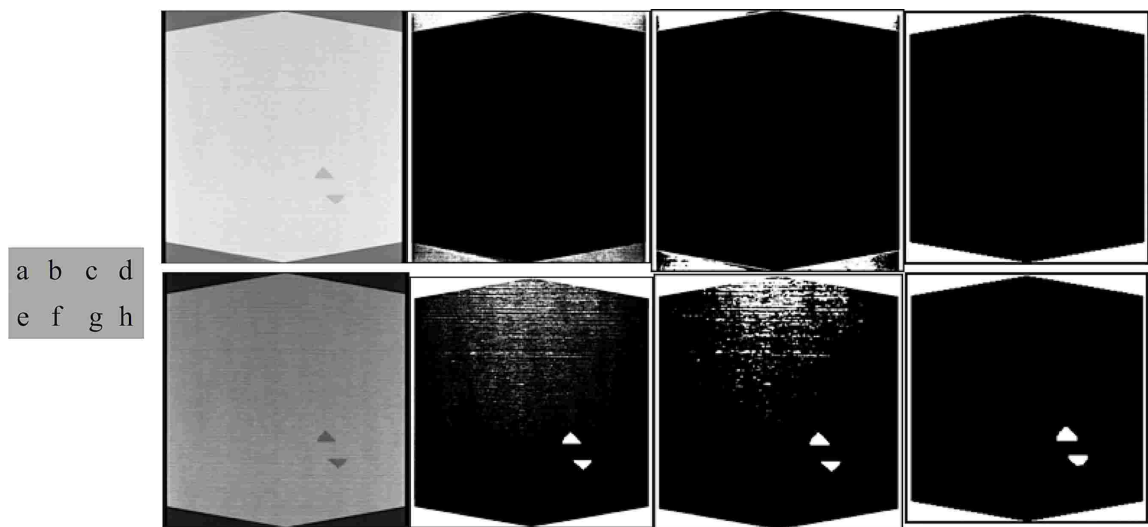We were able to effectively segment out cracks and delamination by using the three FiND CNN models. The development of the three different Views enabled us to consider three different perspectives of the same RIO while consolidating the Views information into a data format that was easily ingested into the models without adding irrelevant and losing relevant information about the observed RIO.

The focused model is great at picking up fine damage but susceptible to noisy (false positive) pixels. While the distant model is sufficient for delamination but lags on picking up fine detailed damages. And, the Near model is a balance between the Focused and the Distant models. By combining the three models prediction into one colored image, we were able to show a fast and easy identification of isolated cracks while minimizing the noisy pixels. Also, delamination is best predicted with the Distant model as it requires less processing time with sufficient accuracy.

We were able to detect the composite material's outlining edges in the images without affecting the outcome of the prediction. Sometimes, the results of the models are susceptible to the quality and contrast of the CT images which can easily be improved with manual enhancing of the images contrast. However, future work should include developing automatic contrast enhancing techniques.

5.1 Future Work

Continuing efforts to improve the performance of the FiND model and the segmentation techniques should be the priority by including more experiments and developing a robust model. The future work should also include optimizing the algorithms for fast predictions, developing an improved and automated contrast enhancement algorithms, identifying and labeling the different types of anomalies detected within an image, and expanding the training data sets to include more types of damages, porosity, wrinkles, and so forth.

REFERENCES

[1] H. O. Pierson, *Handbook of Carbon, Graphite, Diamond and fullerenes : properties, processing and Applications.* Noyes Publications, 1993.

[2] J. Gorss, "High performance carbon fibers," *American Chemical Society*, 2003.

[3] "Carbonx^TMcarbon fiber pc 3d printing filament." `https://www.3dxtech.com/carbonx-carbon-fiber-pc-3d-printing-filament/`. Accessed: 2018-03-26.

[4] R. UnnÞÓrsson, M. T. Jonsson, and T. P. Runarsson, "NDT METHODS FOR EVALUATING CARBON FIBER COMPOSITES," tech. rep., University of Iceland, 2004.

[5] R. C. Gonzalez and R. W. Woods, *Digital Image Processing.* Pearson Education, Inc., 2008.

[6] J. Banhart, ed., *Advanced Tomographic Methods in Materials Research and Engineering.* Oxford University Press, 2008.

[7] B. Bauer, X. Cai, S. Peth, K. Schladitz, and G. Steidl, "Variational-based segmentation of bio-pores in tomographic images," *Computers & Geosciences*, vol. 98, pp. 1–8, 2017.

[8] W. Krakow, "Image-processing for materials characterization," *Journal of metals*, vol. Vol. 35, pp. A42– A42, 1982.

[9] R. Leach, *Characterisation of areal surface texture.* Springer, 2013.

[10] M. L. Comer and E. J. Delp, "The em/mpm algorithm for segmentation of textured images: analysis and further experimental results," *IEEE Transactions on image processing*, vol. 9, no. 10, pp. 1731–1744, 2000.

[11] L. O. Hall, A. M. Bensaid, L. P. Clarke, R. P. Velthuizen, M. S. Silbiger, and J. C. Bezdek, "A comparison of neural network and fuzzy clustering techniques in segmenting magnetic resonance images of the brain," *IEEE transactions on neural networks*, vol. 3, no. 5, pp. 672–682, 1992.

[12] S. Sarkar, K. K. Reddy, M. Giering, and M. R. Gurvich, "Deep learning for structural health monitoring: A damage characterization application," *The Prognostics and Health Management Society*, 2016.

[13] C. Ruggiero, A. Ross, and R. Porter, "Segmentation and learning in the quantitative analysis of microscopy images," in *Image Processing: Machine Vision Applications VIII*, vol. 9405, p. 94050L, International Society for Optics and Photonics, 2015.

[14] A. Krizhevsky, I. Sutskever, and G. E. Hinton, "Imagenet classification with deep convolutional neural networks," in *Advances in neural information processing systems*, pp. 1097–1105, 2012.

[15] C. D. Lockard, "Anomaly detection in radiographic images of composite materials via crosshatch regression," Master's thesis, Old Dominion University, 2015.

[16] T. F. Chan and L. A. Vese, "Active contours without edges," *IEEE Transactions on image processing*, vol. 10, no. 2, pp. 266–277, 2001.

[17] V. H. C. de Albuquerque, J. M. R. Tavares, and L. M. Durão, "Evaluation of delamination damages on composite plates using techniques of image processing and analysis and a backpropagation artificial neural network," in *EngOpt 2008-International Conference on Engineering Optimization*, 2008.

[18] M. Krumm, C. Sauerwein, V. Hämmerle, R. Oster, B. Diewel, M. Sindel, and A. Audi, "Capabilities and application of specialized computed tomography methods for the determination of characteristic material properties of fiber composite components," in *Conference on Industrial Computed Tomography, Wels, Austria*, pp. 19–21, 2012.

[19] X. Liu and F. Chen, "Defects characterization in cfrp using x-ray computed tomography," *Polymers & Polymer Composites*, vol. 24, no. 2, p. 149, 2016.

[20] M. F. Pernice, N. V. De Carvalho, J. G. Ratcliffe, and S. R. Hallett, "Experimental study on delamination migration in composite laminates," *Composites Part A: Applied Science and Manufacturing*, vol. 73, pp. 20–34, 2015.

[21] E. Yılmaz, M. G. Gökçen, A. Demirural, and T. Baykara, "Characterization of the damage mechanism of composites against low velocity ballistic impact using computed tomography (ct) techniques," *Res Dev Material Sci*, p. 1(5), 2017.

[22] K. Song, F. A. Leone, and C. A. Rose, *Continuum Damage Mechanics Models for the Analysis of Progressive Damage in Cross-Ply and Quasi-Isotropic Panels Subjected to Static Indentation.* American Institute of Aeronautics and Astronautics, 2018.

[23] B. Ingalls, "Aerial view of the washington monument on thursday, april 5, 2012 in washington.." `https://images.nasa.gov/details-201204050005HQ.html`, 2012-04-05.

[24] T. Fawcett, "An introduction to roc analysis," *Pattern recognition letters*, vol. 27, no. 8, pp. 861–874, 2006.

[25] D. Sammons, L. Chen, and R. Milletich, "Summary of results from application of **CNN** to nasa image data," white paper, NASA Langley Research Center, Office of the Chief Information Officer, Hampton, Virginia, October 2016.

[26] J. Behnsen, O. O. Blake, R. J. Cernik, and P. J. Withers, "Identifying microcracks in multi-phase crystalline rocks by x-ray ct," *iCT Conference*, 2014.

[27] T. S. Sprague, *X-ray tomography for evaluation of damage in concrete bond.* PhD thesis, University of Washington, 2006.

[28] W. Wang, X. Wan, J. Zhou, M. Zhao, Y. Li, S. Shang, and X. Gao, "Damage and failure of laminated carbon-fiber-reinforced composite under low-velocity impact," *Journal of Aerospace Engineering*, vol. 27, no. 2, pp. 308–317, 2012.

[29] U. K. Bhowmik, D. Mandala, N. W. Hudyma, O. P. Kreidl, and A. Harris, "Segmentation of cracks in x-ray ct images of tested macroporous plaster specimens," in *SOUTHEASTCON 2014, IEEE*, pp. 1–8, IEEE, 2014.

[30] U. K. Bhowmik, T. Cork, and N. W. Hudyma, "Polynomial regression, area and length based filtering to remove misclassified pixels acquired in the crack segmentation process of 2d x-ray ct images of tested plaster specimens," in *Computational Science and Computational Intelligence (CSCI), 2015 International Conference on*, pp. 437–442, IEEE, 2015.

[31] K. Maalmi, A. El-Ouaazizi, R. Benslimane, L. L. Y. Voon, A. Diou, and P. Gorria, "Crack defect detection and localization using genetic-based inverse voting hough transform," in *Pattern Recognition, 2002. Proceedings. 16th International Conference on*, vol. 3, pp. 257–260, IEEE, 2002.

[32] T. M. Meksen, M. Boudraa, and R. Drai, "Detection of cracks in materials using the randomized hough transform on ultrasonic images," in *Proc. of the 6th WSEAS Int. Conf. Signal Processing, Computational Geometry and Artificial Vision*, pp. 202–206, Citeseer, 2006.

[33] T. Merazi-Meksen, M. Boudraa, and B. Boudraa, "Mathematical morphology for tofd image analysis and automatic crack detection," *Ultrasonics*, vol. 54, no. 6, pp. 1642–1648, 2014.

[34] C. Park, J. Z. Huang, J. X. Ji, and Y. Ding, "Segmentation, inference and classification of partially overlapping nanoparticles," *IEEE transactions on pattern analysis and machine intelligence*, vol. 35, no. 3, pp. 1–1, 2013.

[35] H. Ijaz, L. Gornet, M. Khan, W. Saleem, K. Nisar, and S. Chaudry, "Prediction of delamination crack growth in carbon/fiber epoxy composite laminates using a non-local cohesive zone modeling," in *Advanced Materials for Applied Science and Technology II*, vol. 570 of *Advanced Materials Research*, pp. 25–36, Trans Tech Publications, 10 2012.

[36] S.-J. Yoon, D. Chen, S.-W. Han, N.-S. Choi, and K. Arakawa, "Ae analysis of delamination crack propagation in carbon fiber-reinforced polymer materials," *Journal of Mechanical Science and Technology*, vol. 29, no. 1, pp. 17–21, 2015.

[37] B. Yu, R. Bradley, C. Soutis, and P. Withers, "A comparison of different approaches for imaging cracks in composites by x-ray microtomography," *Phil. Trans. R. Soc. A*, vol. 374, no. 2071, p. 20160037, 2016.

[38] E. D. Sosa, E. S. Worthy, and T. K. Darlington, "Microwave assisted manufacturing and repair of carbon reinforced nanocomposites," *Journal of Composites*, vol. 2016, 2016.

[39] H. A. Alessa, *Delamination in hybrid carbon/glass fiber composites*. University of Dayton, 2014.

[40] S. Namata, "Cryogenic durability and finite element analysis of carbon fiber reinforced composites," *J Material Sci Eng*, vol. 4, no. 183, pp. 2169–0022, 2015.

[41] S. Ioffe and C. Szegedy, "Batch normalization: Accelerating deep network training by reducing internal covariate shift," in *International conference on machine learning*, pp. 448–456, 2015.

[42] F. Chollet *et al.*, "Keras." `https://keras.io`, 2015.

[43] M. Abadi, A. Agarwal, P. Barham, E. Brevdo, Z. Chen, C. Citro, G. S. Corrado, A. Davis, J. Dean, M. Devin, S. Ghemawat, I. Goodfellow, A. Harp, G. Irving, M. Isard, Y. Jia, R. Jozefowicz, L. Kaiser, M. Kudlur, J. Levenberg, D. Mané, R. Monga, S. Moore, D. Murray, C. Olah, M. Schuster, J. Shlens, B. Steiner, I. Sutskever, K. Talwar, P. Tucker, V. Vanhoucke, V. Vasudevan, F. Viégas, O. Vinyals, P. Warden, M. Wattenberg, M. Wicke, Y. Yu, and X. Zheng, "TensorFlow: Large-scale machine learning on heterogeneous systems," 2015. Software available from tensorflow.org.

[44] C. Bishop, *Pattern Recognition and Machine Learning.* Springer-Verlag New York, 2006.

[45] F. Pedregosa, G. Varoquaux, A. Gramfort, V. Michel, B. Thirion, O. Grisel, M. Blondel, P. Prettenhofer, R. Weiss, V. Dubourg, J. Vanderplas, A. Passos, D. Cournapeau, M. Brucher, M. Perrot, and E. Duchesnay, "Scikit-learn: Machine learning in Python," *Journal of Machine Learning Research*, vol. 12, pp. 2825–2830, 2011.

VITA

Desalegn Temesgen Delelegn

Department of ELECTRICAL AND COMPUTER ENGINEERING

Old Dominion University

Norfolk, VA 23529

Desalegn received his B.Sc. in Electrical Engineering from Mekelle University, Ethiopia in 2010 and his M.S. in Electrical and Computer Engineering from Old Dominion University in 2018. He is currently pursuing his PhD in Electrical and Computer Engineering at George Mason University.

Desalegn served in the US Navy from March 2011 to January 2017 as a Gas Turbine Technician on board the USS Vella Gulf (CG-72) and later as a leading instructor in the Fabrication Laboratory at Mid-Atlantic Regional Maintenance Center(MARMC). After his honorable discharge from the U.S. Navy in January 2017, he joined NASA Langley Research Center (LaRC) as a Data Science intern. He has participated in numerous projects under the Office of the Chief Information Officer (OCIO), including his MS thesis research . Currently, he is working in the Nondestructive Evaluation Sciences Branch (NESB) as a Data Science intern.

Typeset using LaTeX.